What neutron stars tell about the hadron-quark phase transition: A Bayesian study

János Takátsy[*]

Institute for Particle and Nuclear Physics, Wigner Research Centre for Physics, 1121 Budapest, Hungary
and Institute of Physics, Eötvös University, 1117 Budapest, Hungary

Péter Kovács and György Wolf

Institute for Particle and Nuclear Physics, Wigner Research Centre for Physics, 1121 Budapest, Hungary

Jürgen Schaffner-Bielich

Institut für Theoretische Physik, Goethe Universität Frankfurt, D-60438 Frankfurt, Germany

The existence of quark matter inside the heaviest neutron stars has been the topic of numerous recent studies, many of them suggesting that a phase transition to strongly interacting conformal matter inside neutron stars is feasible. Here we examine this hybrid star scenario using a soft and a stiff hadronic model, a constituent quark model with three quark flavors, and applying a smooth crossover transition between the two. Within a Bayesian framework, we study the effect of up-to-date constraints from neutron star observations on the equation-of-state (EOS) parameters and various neutron star observables. Our results show that a pure quark core is only possible if the maximum mass of neutron stars is below $\sim 2.35 M_\odot$. However, we also find, consistent with other studies, that a peak in the speed of sound, exceeding $1/3$, is highly favored by astrophysical measurements, which might indicate the percolation of hadrons at ~ 3–$4 n_0$. Even though our prediction for the phase transition parameters varies depending on the specific astrophysical constraints utilized, the position of the speed of sound peak only changes slightly, while the existence of pure quark matter below $\sim 4 n_0$, using our parametrization, is disfavored. On the other hand, the preferred range for the EOS shows signs of conformality above $\sim 4 n_0$. Additionally, we present the difference in the upper bounds of radius estimates using the full probability density data and sharp cutoffs and stress the necessity of using the former.

I. INTRODUCTION

Neutron stars (NSs) are one of the end points of stellar evolution formed in core-collapse supernovae with a progenitor mass of $8 M_\odot$ or more. NSs are so compact that the central energy density can reach several times the one of nuclear matter at saturation. At these high densities, new particles could emerge and/or matter is transformed to a new phase characterized by approximate chiral symmetry restoration, which is dubbed the hadron-quark phase transition (see, e.g., Ref. [1] for an introduction).

In the last few years, observations of NSs revealed several breakthrough measurements of their global properties. So it is now well established that pulsars, rotation-powered NSs, can have masses of around two solar masses [2–6], as determined from the timing of the pulses of NSs in binary systems with corrections from general relativity, such as the pulsar PSR J0740 + 6620 with a mass of $M = 2.08 \pm 0.07 M_\odot$ [6]. NSs with a low-mass stellar companion, so-called black-widow or redback pulsars, can have even higher masses. These masses are extracted from the observation of the stellar companion and amount to $M = 2.11 \pm 0.04 M_\odot$ for PSR J1810 + 1744, $M = 2.22 \pm 0.10 M_\odot$ for PSR 1311-3430, and even $M = 2.35 \pm 0.17 M_\odot$ for PSR J0952-0607 [7–9].

Furthermore, the mass and radius of NSs could be constrained directly with the phase-resolved observations of the hot spots on the surface of the NS with the NICER mission for PSR J0030 + 0451 [10–12] and PSR J0740 + 6620 [13–15]. Analysis of the gravitational wave (GW) event GW170817 of a binary NS merger reveals that NSs must have a rather small radius. The limit on the tidal deformability inferred from the GW has been extracted for low and high spins of the merging NSs and under different assumptions of the property of NS matter, i.e., the equation of state (EOS) by the LIGO/Virgo scientific collaboration [16–18]. The limit on the radius has been

[*]takatsy.janos@wigner.hu

inferred by various groups to be less than $R \leq$ 13.2–13.7 km for a $1.4M_\odot$ NS (see Refs. [19–22]).

Because of the high densities present in the cores of the most massive NSs, it is possible that hybrid stars exist with cores containing deconfined quark matter. The possibility of such a hadron to quark phase transition in NSs has been the topic of numerous recent studies. Many of them have investigated the impact of a strong first-order phase transition on astrophysical observables [23,24], as such a phase transition is proposed by effective quark-meson models. However, recent astrophysical measurements seem to rule out strong first-order phase transitions at low densities, while making their existence unlikely at higher densities as well [25–28]. Another way to look for an indication of deconfinement inside NSs is to investigate if the conformal limit is approached. Multiple studies suggest that the existence of conformal matter inside NSs is feasible, which might indicate the existence of hybrid stars [29,30]. Contrary to a first-order phase transition, many recent studies propose an alternative scenario with a peak appearing in the speed of sound and reaching above the conformal limit [30–32]. This possibility is naturally achieved in models of the so-called quarkyonic matter (e.g., [33,34]). Recent investigations of color superconductivity using functional methods also independently found such a peak in their models [35–37].

Despite recent developments in the fields of the complex Langevin method or alternative expansion schemes [38–40], the sign problem still poses a huge challenge for first-principle calculations of quantum chromodynamics (QCD). Therefore, when trying to describe strongly interacting matter at finite densities and low temperature, an effective treatment of the strong degrees of freedom is reasonable.

The nuclear EOS below saturation density is well established. Here, two- and three-body interactions are determined by experimental data mostly based on nucleon-nucleon scattering and properties of light nuclei (e.g., [41,42]). For these microscopic methods, the source of uncertainties usually stems from the interactions applied, as well as the calculation methods themselves [43,44]. In addition to higher-body interaction becoming more important at higher densities, one might also need to account for new degrees of freedom, such as hyperons or quarks. Chiral effective field theory (EFT) provides a robust way to estimate these uncertainties [45,46]. According to state-of-the-art calculations, the uncertainties of the nuclear EOS above $\sim 1.1 n_0$ become increasingly significant, with n_0 being the baryon density at nuclear saturation [47,48]. Hadron resonance gas models provide a different way to calculate the low-density EOS, while accommodating lattice data [49,50]. Another common way to account for the low-density behavior of hadronic matter is to apply a relativistic mean field model with parameters set by nuclear properties at saturation (e.g., [51–53]).

On the opposite side of the phase diagram, at very high densities, due to the asymptotic freedom, one can resort to perturbative QCD methods [54,55]. This area, however, despite what its name might suggest, is remarkably challenging due to an infinite number of diagrams that need to be accounted for at a given order. In fact in the past several decades, only few advancements have been reported in this field, with recent studies calculating the leading contributions to N^3LO [56]. Considering the zero temperature EOS, this method gives reliable results at $\mu_B \gtrsim 2.5$ GeV, or equivalently, $n_B \gtrsim 40 n_0$.

Therefore, there is more than an order of magnitude in density, where the EOS is largely uncertain. Several approaches exist in this region as well, apart from the ones that extrapolate from saturation properties of nuclear matter [57], one might also use Nambu–Jona-Lasinio (NJL) or linear sigma-type models, which are based on the global symmetries of QCD, especially on chiral symmetry and the premise of chiral symmetry restoration at high densities (e.g., [58–62]). In this region, the phase boundaries are also ambiguous. Quark deconfinement can occur at virtually any densities in this uncertain domain, while there are also strong indications for the existence of a color superconducting phase at densities reachable inside the cores of massive NSs [63–65]. Extensive studies of the NJL-type models exist in the literature, with nonlocal interactions also being considered in recent studies [66–68].

Many recent studies investigate this topic in a model-agnostic way, using general, parametrized equations of state [29,32,69,70] or using a constant speed of sound construction, with no underlying microphysical input for the quark part of the EOS [71,72]. In this paper, we instead utilize equations of state derived from a $U_L(3) \times U_R(3)$ chirally symmetric constituent quark-meson model developed by our group [73–76]. At zero density and finite temperature, this model manages to comply with lattice results remarkably well [74], while the parameters of this model are also carefully determined using meson vacuum phenomenology, which is not typical of similar studies. This way, our approach incorporates physical constraints from vacuum phenomenology and QCD thermodynamics at finite temperature. On the other hand, NS observations provide additional constraints for our model parameters undetermined by the parametrization. We use a hybrid approach in describing NSs with quark cores, utilizing relativistic mean field models at low densities [the Steiner-Fischer-Hempel (SFHo) and the density-dependent (DD2) models [51–53]], equations of state from our constituent quark model at high densities, while a smooth interpolation is applied between the two parts. Similar studies, using NJL-type models, are also available in the literature (see, e.g., Refs. [77–80]). We are going beyond previous works by utilizing a general concatenation scheme and presenting an in-depth analysis of the allowed parameter regions of our constituent quark model, including the most recent

astrophysical constraints. We also investigate how our results compare to studies using a model-agnostic approach.

This paper is organized in the following way. In Sec. II, we review the method we used to construct hybrid equations of state for cold NS matter, then after summarizing recent results from NS observations we introduce our Bayesian framework. In Sec. III, we show the results from our Bayesian analysis and demonstrate how different astrophysical measurements influence the outcome of these.

II. METHODS

In this section, we first review how our hybrid EOS is constructed, then after an overview of the calculation of NS observables and recent observations, we proceed to describe the details of our Bayesian analysis, devoting special attention to how our posterior probabilities are calculated.

A. Equation of state

To be able to investigate the effect of variations in the properties of our quark model on stable sequences of NSs, we need to construct a reliable EOS covering a large range in density from below saturation density up to $n_B \approx 5$–$6n_0$, where n_0 is the baryon density at nuclear saturation.

As already mentioned in Sec. I, we use a hybrid approach, combining equations of state from hadronic and quark matter. For the hadronic part, we use two relativistic mean field models, the Steiner-Fischer-Hempel model [51] and the density-dependent model of Typel *et al.* [52,53]. We obtained both equations of state from the CompOSE database [81]. Both models are consistent with chiral EFT calculations at low densities,[1] but differ in the stiffness at higher densities; while the SFHo EOS is relatively soft, the DD2 EOS is quite stiff, with maximally stable NS masses of $\sim 2.05 M_\odot$ and $\sim 2.42 M_\odot$, respectively.

For the quark part, we utilize the (axial) vector meson extended linear sigma model (eLSM), developed and thoroughly investigated in several previous papers [73–76] with investigations about the large-N_c behavior as well [87]. This is a three-flavor quark-meson model containing constituent quarks and the complete nonets of (pseudo)scalar and (axial) vector mesons. The advantage of this model—altogether with the parametrization procedure and the approximations that were used—is that it reproduces the meson spectrum (and also various decay widths) quite well at $T = \mu_B = 0$, and moreover, its finite temperature version also agrees well with various lattice results [74]. The detailed description of the approximation we use in this paper can be found in

Ref. [88], where we have also already provided a comparison between the sequences of static (nonrotating) NSs predicted by the model and astrophysical observations.

It is worth noting that, due to various particle mixings in the scalar sector, there is more than one possibility to assign scalar mesons to experimental resonances [73]. Possibly stemming from this mixing is that the mass of the sigma meson needs to be very low in our model in order to achieve a correct finite temperature behavior and to reproduce other meson masses correctly. This problem might be resolved by considering additional bound quark states, such as tetra-quarks. However, as we showed in Ref. [88], this low sigma meson mass, within the framework of this model, is also consistent with astrophysical observations.

Nevertheless, similar to the analysis in Ref. [88], we leave m_σ as a free parameter and let it vary between 290 and 700 MeV. Another important parameter, which is not fixed by experimental data in the approximation we use, is the coupling between vector mesons and constituent quarks. We vary this parameter in the range $g_V \in [0, 10]$.

Since the low- and high-density models operate with different degrees of freedom, we need to utilize some effective method to arrive from one phase to another. The simplest way to do this, which we will also follow in our paper, is to simply interpolate between the two zero temperature equations of state in some intermediate-density region (see, e.g., Refs. [89–92]). Also similar to other studies, we use a polynomial interpolation; however, in contrast to using the pressure $p(\mu_B)$ as a thermodynamic potential for the interpolation, we use the energy density $\varepsilon(n_B)$. We do this, since we find that this way the sound speed in the intermediate region shows a less sharp peak, and therefore a larger ensemble of equations of state will turn out to be causal.

In case the hadronic EOS $\varepsilon_{\mathrm{H}}(n_B)$ is valid up to n_{BL}, and the quark EOS $\varepsilon_{\mathrm{Q}}(n_B)$ can be utilized above n_{BU}, the interpolating polynomial looks like

$$\varepsilon(n_B) = \sum_{k=0}^{N} C_k n_B^k, \qquad n_{BL} < n_B < n_{BU}, \qquad (1)$$

where the coefficients C_k are determined so that the energy density and several of its derivatives remain continuous in the whole region. In our case, we use a fifth-order polynomial, so we need the energy density and its first and second derivatives to be continuous at the boundaries. The first derivative of the energy density with respect to the baryon number density is the baryon chemical potential, so this condition will ensure that the pressure is also continuous at the boundaries. The condition for the second derivative, in addition, ensures a continuous speed of sound.

From n_{BL} and n_{BU} we define the central density and width of the phase transition as $\bar{n} = (n_{BU} + n_{BL})/2$ and $\Gamma = (n_{BU} - n_{BL})/2$, respectively.

---

[1]See, e.g., Fig. 9 of Ref. [82] at the relevant density above $\sim 0.5 n_0$, below which the EOS is strongly influenced by nuclear clustering, and thus the proper crust EOS has to be used [57,83–85], which we extracted from the unified EOS by Douchin and Haensel [86].

As a further remark, we add that a Maxwell construction is also a common way to get from one phase to the other; however, this method limits the possible range of concatenations by requiring the $p(\mu_B)$ curves of the two phases to cross each other and also removes the freedom of choosing the density at which the phase transition occurs. From a philosophical point of view, one might also argue that since both models have a limited region of validity, at intermediate densities one can only assume some interpolation between the two models.

B. Neutron stars and observations

Here we briefly summarize how one can calculate different equilibrium properties of NSs given a specific EOS. For details of these calculations, we refer the reader to Ref. [88], as well as references therein.

Once we have an EOS $p(\varepsilon)$, we can obtain mass-radius relations of NSs by solving the Tolman-Oppenheimer-Volkoff equations [93,94],

$$\frac{\mathrm{d}m(r)}{\mathrm{d}r} = 4\pi r^2 \varepsilon(r), \tag{2}$$

$$\frac{\mathrm{d}p(r)}{\mathrm{d}r} = -[\varepsilon(r) + p(r)]\frac{m(r) + 4\pi r^3 p(r)}{r^2 - 2m(r)r}, \tag{3}$$

where $m(r)$ is the gravitational mass enclosed within a sphere with radius r, and $p(r)$ is the pressure related to the energy density $\varepsilon(r)$ by the EOS. These equations can usually only be integrated numerically. The total mass (M) and radius (R) of the NS for a certain central energy density ε_c is obtained through the boundary conditions, $\varepsilon(r = 0) = \varepsilon_c$, $p(R) = 0$, and $m(R) = M$.

Another property of NSs that is becoming more and more important due to the recent and future observations of inspirals of NSs with GW detectors is the λ tidal deformability parameter (e.g., [16,95,96]). This parameter is related to the k_2 quadrupole tidal Love number through

$$k_2 = \frac{3}{2}\lambda R^{-5}, \tag{4}$$

where k_2 can usually be obtained by numerical integration (see, e.g., Refs. [95,97–99]). The dimensionless parameter $\tilde{\Lambda}$ measurable through GW observations of binary NSs can then be calculated by

$$\tilde{\Lambda} = \frac{16}{13}\Lambda_1 \frac{M_1^4}{M_{\mathrm{tot}}^4}\left(12 - 11\frac{M_1}{M_{\mathrm{tot}}}\right) + 1 \leftrightarrow 2, \tag{5}$$

where $M_{\mathrm{tot}} = M_1 + M_2$, and where $\tilde{\Lambda}$ is directly determined by the phase shift in the GW signal of circular NS binaries due to tidal effects [100]. Here Λ_i is the dimensionless tidal parameter of component i, which can be obtained through

$$\Lambda_i = \frac{\lambda_i}{M_i^5}. \tag{6}$$

There are already several stringent observational constraints on what the EOS should look like, with more expected to come in the near future. These constraints stem from various sources, such as electromagnetic, GW, or combined, multimessenger observations.

Masses of NSs, in case they form a binary with an other object, might be measured with remarkable precision, using, for example, the Shapiro time delay effect. In the past decade, multiple highly massive NSs have been observed, providing robust constraints on the stiffness of the EOS [101–103]. From these, until recently, the most massive was PSR J0740 + 6620, with a mass of $2.08 \pm 0.07 M_\odot$ and a 95.4% lower bound of $1.95 M_\odot$ [104]. Since then, however, several other observations have also raised notable interest [7,105]. Observations of the black-widow pulsar PSR J0952-0607 have measured its mass to be $2.35 \pm 0.17 M_\odot$ [8].

A recent observation discovered a very light central compact object within the supernova remnant HESS J1731-347. It can either be interpreted as the lightest NS observed so far, or a quark star with a mass of $0.77^{+0.20}_{-0.17} M_\odot$ and radius $10.4^{+0.86}_{-0.78}$ km.

Unlike masses, the measurement of radii of NSs is extremely challenging, and so far, the most accurate x-ray measurements were able to achieve a precision of $\sim$10%. Recent measurements of the NICER Collaboration use the ingenious idea of examining the rotation-resolved x-ray spectrum of NSs with hot spots. This, for the first time, enables the simultaneous measurement of the mass and radius of a single NS. Two NSs have been measured with this method so far, one is PSR J0030 + 0451 with a mass and equatorial radius of $1.44^{+0.15}_{-0.14} M_\odot$ and $13.02^{+1.24}_{-1.06}$ km [106] or $1.34^{+0.15}_{-0.16} M_\odot$ and $12.71^{+1.14}_{-1.19}$ km [107], according to different collaborations using slightly different methods. The other pulsar measured was the massive pulsar PSR J0740 + 6620, with mass $2.08 \pm 0.07 M_\odot$ and reported radii of $13.7^{+2.6}_{-1.5}$ km [108] or $12.39^{+1.30}_{-0.98}$ km [109] at the 68% credible interval.

In addition to these measurements, we have also witnessed the first multimessenger observation of a binary NS merger, with its GW signal being labeled GW170817. The first analysis of GW170817 performed by the LIGO-Virgo Collaboration (LVC) inferred a value of $\Lambda < 800$ for $1.4 M_\odot$ NSs in the low-spin limit [16]. A thorough investigation of this constraint performed by Ref. [19] using a generic family of equations of state found an upper radius limit of 13.6 km for $1.4 M_\odot$ NSs, while Ref. [20] arrived at a radius limit of 13.7 km with higher statistics. A subsequent study was also performed by the LVC, in which a combined analysis of tidal deformabilities and NS radii was performed, utilizing various assumptions for the equations

of state. Here the values of $\Lambda(1.4M_\odot) = 190^{+390}_{-120}$ and $R(1.4M_\odot) = 10.8^{+2.0}_{-1.7}$ km were found [17]. An additional assumption of this study was to use a single EOS to describe both objects, whereas in Ref. [16] the two equations of state were varied independently. A similar study, also using a single EOS ansatz, was performed by Ref. [21], where the authors arrived at a slightly higher upper limit ($\Lambda < 642$, $\Lambda < 698$, or $\Lambda < 681$ depending on the prior assumption on the component masses). A companion study of Ref. [17] was also published by the LVC at around the same time, where an EOS agnostic approach was applied [18]. In their study, they investigated the effect of using various waveform templates, and under minimal assumptions they found for the upper limit of the tidal deformability $\Lambda(1.4M_\odot) < 720$ [18].

In this paper, we chose to utilize the results of this analysis with the upper limit of $\Lambda(1.4M_\odot) < 720$. The minimal prior assumptions of this study make it suitable to use it as a conservative upper limit for the tidal deformability. Other recent studies also utilize this constraint (e.g., [110]). Reference [111] examines previous studies [17,18,21,112,113], investigates the impact of prior assumptions, and argues that upper and especially lower limits on Λ can be misleading without a more detailed discussion. Another reanalysis has also been done by Dietrich *et al.*, which found similar upper limits for Λ (see Table S2 of Ref. [114]).

The electromagnetic properties of the source of GW170817 were also used to put constraints on NSs. A lower radius constraint was inferred by Ref. [115] from the absence of prompt collapse during this event, while an upper mass limit of $2.16^{+0.17}_{-0.15}M_\odot$ was proposed by Ref. [116] using a quasiuniversal relation between the maximum mass of static and the maximum mass of uniformly rotating NSs. This conclusion rests upon the assumption that the merging NSs first formed a differentially rotating hypermassive NS and not a uniformly rotating supermassive one. This hypothesis is supported by simulations of the dynamical ejecta and kilonova modeling (e.g., [117]), albeit other scenarios are not completely ruled out either.

The GW signal of another binary NS merger GW190425 was also observed by the LVC, however, no clear tidal signature or electromagnetic signal was measured. Because of this, the binary NS classification only rests on the estimated masses of the binary components. Yet another notable GW event was GW190814, where one of the binary components resided in the so-called mass gap, with a mass of $2.5 - 2.67M_\odot$ [118], which could either mean it was the lightest black hole (BH) or the heaviest NS observed. Although the NS scenario seems unlikely, it should not be ruled out until further evidence is found against it.

Several studies exist that combine all these astrophysical measurements with nuclear physics and heavy-ion data to give stringent constraints on the nuclear EOS and the $M - R$ relation of NSs (e.g., [113,119–124]). Bayesian investigations are also available in this field (e.g., [32,70,78,79]), while other studies use deep neural networks to constrain the EOS [125,126]. In this paper, we also apply a Bayesian approach. However, we concentrate on hybrid stars, where the properties of quark matter are calculated from an effective model of QCD, with the correct behavior at zero density and finite temperature. Among others, we focus on the restriction of quark model parameters, the parameters of the concatenation, and the conditions for the existence of a pure quark core.

C. Bayesian inference

Suppose our EOS, and hence the properties of NSs, can be described by a set of parameters ϑ. The probability of specific data being measured, given a specific EOS, is $p(\text{data}|\vartheta)$. Then we can use Bayes' theorem to determine the probability of a specific parameter set, given data from a measurement,

$$p(\vartheta|\text{data}) = \frac{p(\text{data}|\vartheta)p(\vartheta)}{p(\text{data})}, \tag{7}$$

where $p(\vartheta)$ is our prior assumption about the parameter sets, and $p(\text{data})$ is just a normalization constant.

Our parameter space consists of the four parameters: m_σ, g_V, $\bar{n}$, and Γ. We vary $\bar{n}$ between $2n_0$ and $5n_0$, Γ between n_0 and $4n_0$, and g_V between 0 and 10. In order to vary m_σ, we need to reparametrize our model, which is computationally expensive and even conceptually different since we end up with a reparametrized model, which is not needed if we change other parameters of the model. Therefore, we do not vary the sigma meson mass continuously, but rather choose five different values for m_σ: 290 MeV, from the original parametrization of the eLSM [88], as well as 400, 500, 600, and 700 MeV. We sample the other three parameters on a grid. Many Bayesian studies apply a Markov chain Monte Carlo approach with the appropriate sampler to obtain the posterior distributions of the model parameters [112]. However, due to the low dimensionality of our parameter space, sampling the parameters on a grid in advance is justified. Many recent Bayesian studies also utilize such a presampled set of equations of state [114,119,127]. Sampling the model parameters on a grid is also not unprecedented (see, e.g., [78,127]) and is justified by the discretized values we take for m_σ. We choose the *a priori* probability for all parameter sets to be equal; hence, in this sense, our prior can be considered nearly uniform in our four-dimensional parameter space.

The equations of state generated using these parameters still need to comply with some basic requirements. We ensure that the low-density EOS is described by the hadronic EOS by discarding parameter sets with $\bar{n} - \Gamma < n_0$. Additionally, we require stability and causality for all equations of state. Ultimately, we end up with a set of

~18000 equations of state, for which the posterior probabilities are calculated.

In addition to our choice for prior in the parameter space, when calculating posterior probabilities for different astrophysical observations, the prior for the NS mass distribution is assumed to be uniform. We note here that a choice for the NS mass prior that does not match the observed distribution can lead to large biases in the Bayesian inference after $\mathcal{O}(25)$ observational events (see, e.g., Refs. [128,129]). For the time being, we can safely assume a uniform prior without having to worry about these biases. Eventually, however, a self-consistent hierarchical framework that simultaneously models equations of state and NS populations will be necessary [130]. For further discussion about the uniform population prior, we refer the reader to Refs. [130–132].

The conditional probability $p(\text{data}|\boldsymbol{\vartheta})$ can be obtained as a product of several independent astrophysical observations,

$$p(\text{data}|\boldsymbol{\vartheta}) = p(M_{\max}|\boldsymbol{\vartheta})p(\text{NICER}|\boldsymbol{\vartheta})p(\tilde{\Lambda}|\boldsymbol{\vartheta}), \quad (8)$$

where we detail the specific observational constraints below. Also note that, since only the proportions of the probabilities for different parameter sets are meaningful, we can neglect constant normalization factors in front of our conditional probabilities.

1. Compatibility with perturbative QCD

Even without any astrophysical constraints, our EOS should comply with some basic physical requirements. First and foremost, our EOS should be causal, meaning

$$c_s^2 = \frac{\mathrm{d}p}{\mathrm{d}\varepsilon} \le 1. \quad (9)$$

In addition, however, we can also use input from perturbative QCD calculations, similar to Refs. [133,134]. We know that at some density n_{QCD} strongly interacting matter should have a baryon chemical potential μ_{QCD} and a pressure p_{QCD}. On the other hand, we require our hybrid EOS to be valid up to the density present in the center of the most massive NS described by that specific EOS. This point is described by n_{NS}, μ_{NS}, and p_{NS}. However, these equations of state should be in accord with each other and therefore there should exist a thermodynamically allowed connection of the two. Therefore, we assume in the core of NSs that $\mu_{\text{NS}} \le \mu_{\text{QCD}}$ and require stability and causality,

$$n_{\text{NS}} \le n_{\text{QCD}}, \qquad p_{\text{NS}} \le p_{\text{QCD}}, \quad (10)$$

$$\frac{n_{\text{NS}}}{\mu_{\text{NS}}} \le \frac{n_{\text{QCD}}}{\mu_{\text{QCD}}}, \quad (11)$$

where we used the fact that a causal EOS crossing the point (μ, n) has a slope $\mathrm{d}n/\mathrm{d}\mu \ge n/\mu$.

We obtain an additional integral constraint from the definition of the difference in pressure,

$$\Delta p = p_{\text{QCD}} - p_{\text{NS}} = \int_{\mu_{\text{NS}}}^{\mu_{\text{QCD}}} n(\mu)\mathrm{d}\mu. \quad (12)$$

The integral here depends on the specific way we connect the two points; however, it can be easily shown that it falls between the two limiting cases (see, e.g., Ref. [133]),

$$\Delta p_{\min} \le \Delta p \le \Delta p_{\max}, \quad (13)$$

with

$$\Delta p_{\min} = \frac{\mu_{\text{QCD}}^2 - \mu_{\text{NS}}^2}{2} \frac{n_{\text{NS}}}{\mu_{\text{NS}}}, \quad (14)$$

$$\Delta p_{\max} = \frac{\mu_{\text{QCD}}^2 - \mu_{\text{NS}}^2}{2} \frac{n_{\text{QCD}}}{\mu_{\text{QCD}}}. \quad (15)$$

For the perturbative QCD EOS, we use the values calculated by Ref. [135] and utilized in Ref. [133] with a renormalization scale parameter $X = 2$; hence, $\mu_{\text{QCD}} = 2.6$ GeV, $n_{\text{QCD}} = 6.47\ 1/\text{fm}^3$, and $p_{\text{QCD}} = 3823\ \text{MeV}/\text{fm}^3$.

2. Mass constraints

We use PSR J0348 + 0432 with a mass $2.01 \pm 0.04 M_\odot$ and PSR J1614-2230 with a mass $1.908 \pm 0.016 M_\odot$ to put a lower limit on the maximum mass of NS mass-radius relations. In order to avoid double counting, we do not include here the mass measurement of PSR J0740 + 6620, since it is included as a NICER measurement. We also similarly include the upper mass bound from Ref. [116]. We then approximate the likelihood functions by error functions,

$$p(M_{\max}|\boldsymbol{\vartheta}) \propto \prod_{i=1,2} \frac{1}{2}\left[1 + \text{erf}\left(\frac{M_{\max}(\boldsymbol{\vartheta}) - M_i}{\sqrt{2}\sigma_i}\right)\right]$$
$$\times \frac{1}{2}\left[1 - \text{erf}\left(\frac{M_{\max}(\boldsymbol{\vartheta}) - M_U}{\sqrt{2}\sigma_U}\right)\right], \quad (16)$$

where erf is the error function. For the upper mass limit from the hypermassive NS scenario, we use $M_U = 2.16 M_\odot$ and set the standard deviation conservatively to $\sigma_U = 0.17 M_\odot$, while $M_1 = 2.01 M_\odot$, $\sigma_1 = 0.04 M_\odot$ and $M_2 = 1.908 M_\odot$, $\sigma_2 = 0.016 M_\odot$.

3. NICER measurements

For the two NICER measurements, we use the kernel density estimated probability density $p_N(M, R)$, utilizing

the data provided by Refs. [106,108]. The likelihood for a single measurement is then given by

$$p(\text{NICER}|\boldsymbol{\vartheta}) \propto \int dM dR \, p_{\text{N}}(M, R) \delta(R - R(M, \boldsymbol{\vartheta}))$$

$$= \int dM \, p_{\text{N}}(M, R = R(M, \boldsymbol{\vartheta})). \qquad (17)$$

Note that the uniform mass population prior is already included in this formula.

4. Tidal deformability measurement

The chirp mass of the source of GW170817 was measured very precisely by the LVC to be

$$\mathcal{M} = \frac{(M_1 M_2)^{3/5}}{(M_1 + M_2)^{1/5}} = (1.186 \pm 0.001) M_\odot, \quad (18)$$

where M_1 is conventionally considered to be the mass of the NS with the larger mass. We then use the joint posterior probability density $p_{\text{GW}}(\tilde{\Lambda}, q)$, provided by Ref. [118], where $q = M_1/M_2$ is the mass ratio. The accurate measurement essentially determines the secondary mass M_2 for a specific primary mass M_1. Then, utilizing the EOS, Λ_1 and Λ_2 can be determined and therefore $\tilde{\Lambda}$ as well. We then calculate the conditional probability as

$$p(\tilde{\Lambda}|\boldsymbol{\vartheta}) \propto \int_{M_{\text{eq}}}^{M_{\text{max}}} dM_1 \, p_{\text{GW}}(\tilde{\Lambda}(M_1, \mathcal{M}, \boldsymbol{\vartheta}), q(M_1, \mathcal{M})), \qquad (19)$$

where $M_{\text{eq}} = 1.362 M_\odot$ corresponds to a mass ratio of $q = 1$, and M_{max} is the mass of the maximally stable NS.

5. BH hypothesis

Based on some properties of the electromagnetic counterpart of GW170817, some previous works have suggested that the remnant collapsed to a BH (e.g., [116,117,136]). We refer to this as the BH hypothesis. In order to incorporate this assumption in our analysis, we utilize baryon number conservation during the merger event,

$$N_1 + N_2 = N_{\text{remn}} + N_{\text{ej}}, \qquad (20)$$

where N_1 and N_2 are the baryon numbers of the two component NSs, while N_{remn} and N_{ej} are the baryon numbers corresponding to the remnant and the ejecta, respectively. Similar to Refs. [110,134], we use the assumption $N_{\text{ej}} \approx 0$. Hence, in order for the remnant to collapse to a BH we must have $N_1 + N_2 > N_{\text{max}}$, where N_{max} is the baryon number of the maximally massive stable NS. To add this assumption to our analysis, we discard every pair of NSs during the integral in Eq. (19), for

which $N_1 + N_2 \leq N_{\text{max}}$. Since values that $N_1 + N_2$ can take are primarily determined by experiment and higher values become more and more improbable, this gives an upper bound for $N_1 + N_2$, which, in turn, gives an upper bound on the maximum mass of NSs, $M_{\text{max}} \lesssim 2.53 M_\odot$.

Somewhat more speculatively, one can assume that the remnant for a brief time remained a hypermassive NS, after which it quickly collapsed to a BH (e.g., [116]). We implement this assumption using the upper mass bound M_U mentioned earlier in this section. We refer to this scenario as the hypermassive NS hypothesis.

In addition, we can include the assumption that the inspiral did not end in a prompt collapse to a BH. In this case, we discard pairs of NSs, for which the total mass is above the threshold mass for prompt collapse to a BH. We use this assumption in all of our results that include the BH constraint in any form. Several approaches exist to calculate this threshold mass [137,138]. Here we utilize the nonlinear relation given by Ref. [138], calibrated by numerical relativity simulations,

$$\frac{M_{\text{th}}}{M_{\text{max}}} = a - \frac{b}{1 - c \cdot C_{\text{max}}}, \qquad (21)$$

where $C_{\text{max}} = M_{\text{max}}/R_{\text{max}}$ is the compactness of the maximum mass configuration, and the parameters are $b = 1.01$, $c = 1.34$, and $a = 2b/(2 - c)$. Hence, we only perform the integration in Eq. (19) for configurations where $M_{\text{tot}} = M_1 + M_2 < M_{\text{th}}$.

6. Mass-gap compact object

As we discussed in Sec. II B, an object in the mass gap was observed in the event GW190814 with a mass $M = 2.59^{+0.08}_{-0.09} M_\odot$ in the 90% credible interval [118]. In our analysis, we also investigate what happens when we require this object to be described as a NS. We use a similar error function as for the other mass constraints with a mean $M_{\text{gap}} = 2.59 M_\odot$ and a standard deviation $\sigma_{\text{gap}} = 0.055 M_\odot$, assuming normal distribution.

III. RESULTS

In this section, we discuss our results from our analyses. In Sec. III A, we investigate how well the maximum mass of hybrid stars can be predicted by the parameters of the quark component. In Sec. III B, we show our results from our Bayesian analysis with various constraints included.

A. Dependence of M_{max} on constituent quark model parameters

In Ref. [88] we already showed in selected cases how the maximum mass of hybrid star sequences produced by using the eLSM for the quark component correlates with the parameters chosen for our quark model. Here we also
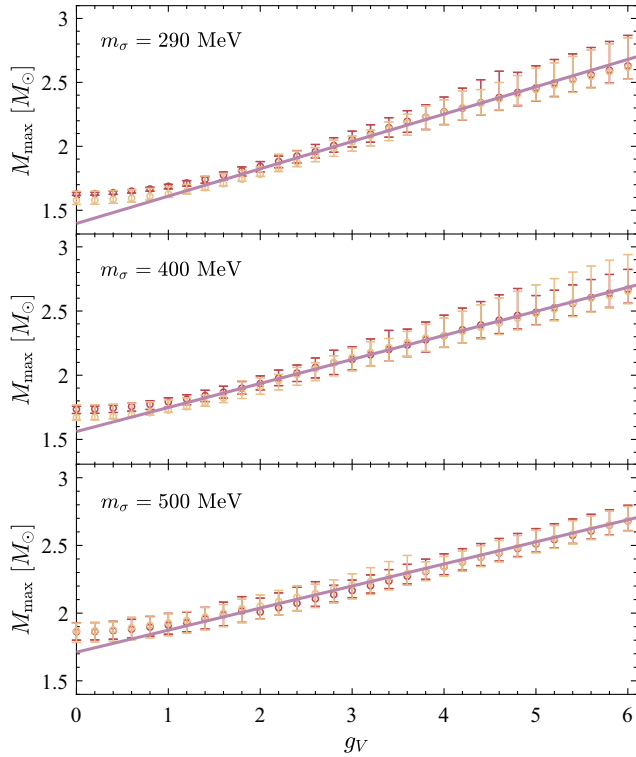
FIG. 1. The maximum mass of stable NSs as a function of the g_V vector meson coupling, for different sigma masses. For specific constituent quark model parameters, the circles denote the median, while the error bars denote the 90% confidence interval of maximum masses obtained by applying the complete ensemble of different concatenation parameters. The two different colors correspond to the SFHo (red) and the DD2 (yellow) hadronic EOS. The fitted relation is visualized by the purple lines.

investigate this correlation on the whole span of the parameter space.

The results are shown in Fig. 1. The three different panels show results for three different values of the sigma meson mass, with $m_\sigma = 290$ MeV being the one preferred by the parametrization. For a specific parameter set $\{m_\sigma, g_V\}$, we have gathered the maximum masses from all the different concatenations and plotted the median and the 90% confidence intervals. The width of these intervals can be even lower than $\pm 0.05 M_\odot$ for $M_{\max} \sim 2M_\odot$, while they moderately increase for higher median masses to $\pm 0.15 - 0.2 M_\odot$. We can also observe that changing the hadronic EOS (red and yellow points) does not make any significant change in the maximum masses.

We try to quantify this correlation by making a linear fit to the points above $g_V = 1$, since below that the dependence is clearly nonlinear. The fitting function is then

$$\frac{M_{\max}}{M_\odot} = \alpha(1 + \gamma \cdot \bar{m}_\sigma) + \beta \cdot g_V(1 + \delta \cdot \bar{m}_\sigma), \quad (22)$$

where

$$\bar{m}_\sigma = \frac{m_\sigma}{500 \text{ MeV}}, \quad (23)$$

and where the cross term with the coefficient δ is necessary since the slope of the linear fit changes for different sigma masses.

The parameters obtained from the fit are

$$\begin{aligned}
\alpha &= 0.962 \pm 0.010, \\
\beta &= 0.284 \pm 0.003, \\
\gamma &= 0.780 \pm 0.013, \\
\delta &= -0.426 \pm 0.014, \quad (24)
\end{aligned}$$

with a goodness-of-fit value $R^2 = 0.952$. The fitted function is shown in Fig. 1 by the purple lines. Because of δ being negative, we get the largest slope for $m_\sigma = 290$ MeV.

B. Bayesian analysis results

During our Bayesian analysis, we incorporate constraints from astrophysical observations in a specific order. After establishing our prior, we include the minimal constraints, namely, the requirement for consistency with perturbative QCD (pQCD) calculations and lower mass limits from the $2M_\odot$ NSs. Then we apply the two NICER measurements, since these are the least constraining on our prior. After that, as another well-established constraint, we apply the tidal deformability measurement of GW170817, which, generally speaking, constrains the radii of $1.4M_\odot$ NSs from above. These measurements constitute our canonical set of constraints.

On top of these, we also investigate the effect of other measurements as well. First, based on the hypermassive NS hypothesis, we put an upper limit on the maximum mass of NSs. As an alternative scenario, we incorporate a weaker constraint, the BH hypothesis, and explore the consequence of assuming the mass-gap object in GW190814 was a very massive NS. Finally, we also briefly review the effect of adding the recent measurement of the light compact object in HESS J1731-347 to our canonical set of constraints on top of the BH hypothesis. During these steps, we try to monitor how the posterior probabilities evolve in the parameter space. We also investigate the radius distribution of $1.4M_\odot$ and $2M_\odot$ NSs during each step. The parameter set with the maximum posterior probability is also determined for each case.

Additionally, we also explore how sharp cutoffs at the 90% credible intervals of measurable quantities from each astrophysical constraint would affect the allowed regions on the mass-radius diagram and compare these results to the ones obtained from the Bayesian analysis. For the $2M_\odot$ constraint, the cut is achieved by requiring $M_{\max} > 1.95 M_\odot$, which corresponds to the two-sigma lower bound for the mass of PSR J0740 + 6620 [6]. For the NICER measurements and the HESS object,

the requirement is that the $M - R$ curves should cross the two-sigma contour lines of the given measurement. The cut for the tidal deformability measurement of GW170817 is established in the following way. For a given EOS, we calculate all the possible $\tilde{\Lambda}$ values between $M_{eq} < M_1 < 1.6 M_\odot$ and keep the EOS if $\tilde{\Lambda} < 720$ for any configuration. Pairs of NSs with $M_{tot} > M_{th}$ are discarded, while pairs with $N_1 + N_2 \leq N_{max}$ are also discarded when the BH hypothesis is included. The upper mass bound from the hypermassive NS hypothesis is taken to be $2.33 M_\odot$, while the lower mass bound from the mass-gap object is taken as $2.5 M_\odot$.

We divide our analysis into two separate parts. First, we restrict the sigma meson mass to $m_\sigma = 290$ MeV and the hadronic EOS to the relatively soft SFHo EOS. This keeps our discussion more transparent when investigating the evolution of probabilities in the parameter space. We also investigate how the predictions change when we use different combinations of the hadronic EOS and m_σ and include the results in tables. For the second analysis, we combine all equations of state with different hadronic equations of state and m_σ and try to draw more general conclusions from the results.

1. Results with the SFHo EOS and $m_\sigma = 290$ MeV

The marginalized priors and posteriors for the three unfixed parameters are shown in Fig. 2. The posteriors correspond to the canonical set of measurements. Even though we have a uniform grid in the parameter space for the prior, due to the requirements for stability and causality, large areas of the parameter space are excluded, and therefore, the marginals appear to have a structure. The posterior for the vector coupling g_V is consistent with our expectations from Sec. III A, considering values below $g_V \approx 3$ become increasingly improbable due to the $2 M_\odot$ constraint. Lower values for $\bar{n}$ and Γ also become disfavored. Even though a figure such as Fig. 2 contains a lot of information about the parameter distributions, due to the marginalized nature of the probability density functions (PDFs) in such a figure, some information is necessarily lost. Therefore, besides the marginalized PDFs shown in Fig. 2, during the following parts of our analysis, we also show different slices of the PDFs in order to analyze the results from a different perspective. We can do this due to the low dimensionality of our parameter space.

We can also explore the effect of different measurements on the mass-radius diagram. The results for our canonical set of measurements are shown in Fig. 3. The left panel shows the results with the minimal constraints. As mentioned before, our prior is taken to be uniform in the parameter space, as it is clearly visible now in the bottom panel, where slices of the PDF for different values of Γ are shown (see the uniform color of the PDFs, apart from the excluded regions). This does not apply to the leftmost region, where parameter sets with low g_V are not preferred
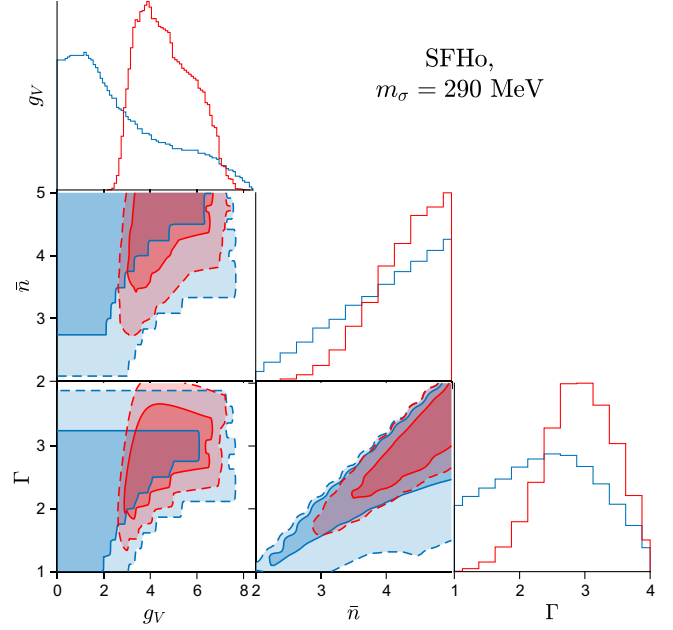

FIG. 2. Marginalized priors (blue) and posteriors (red) for the three unfixed parameters characterizing the constituent quark model and the phase transition. The posterior corresponds to the canonical set of measurements (i.e., the pulsar mass measurements, the NICER measurements, and the tidal deformability measurement of GW170817). For the two-dimensional marginals, the two contours correspond to the 68% (solid) and 95% (dashed) confidence intervals.

by the $2 M_\odot$ constraint. Other regions of zero probability correspond to exclusions. Values of $\bar{n}$ for which $\bar{n} - \Gamma < n_0$ are excluded, since we require our EOS to be described by the hadronic EOS at least up until n_0. The upper right regions with high $\bar{n}$ and g_V are mostly excluded by the instability or acausality of the intermediate interpolated region, and some of them are excluded due to the pQCD constraint. The sharp edges are the result of our finite grid on the parameter space.

Regions of the mass-radius diagram retained after the sharp cutoffs are encompassed by the solid contours. Examining the top left panel, one can observe that the highest mass NSs with masses of $\sim 3.5 M_\odot$ are excluded by the pQCD constraint (see the region between the black and gray contours). Our construction for the EOS results in a stiffening in the intermediate-density region, as we showed in Ref. [88]. A result of this is that even with the relatively soft SFHo model as the hadronic EOS we get radii $R(1.4 M_\odot) \gtrsim 12$ km; hence NSs with $M_{max} \gtrsim 2 M_\odot$ and $R(1.4 M_\odot) \lesssim 12$ km are absent from our prior.

Even though we take a uniform grid on the parameter space, the probability distribution in the $M - R$ plane might still exhibit irregularities, which is visible in the radius distributions as well. During the creation of the probability density plot in the $M - R$ plane, we have to introduce a metric to be able to properly define densities of curves,
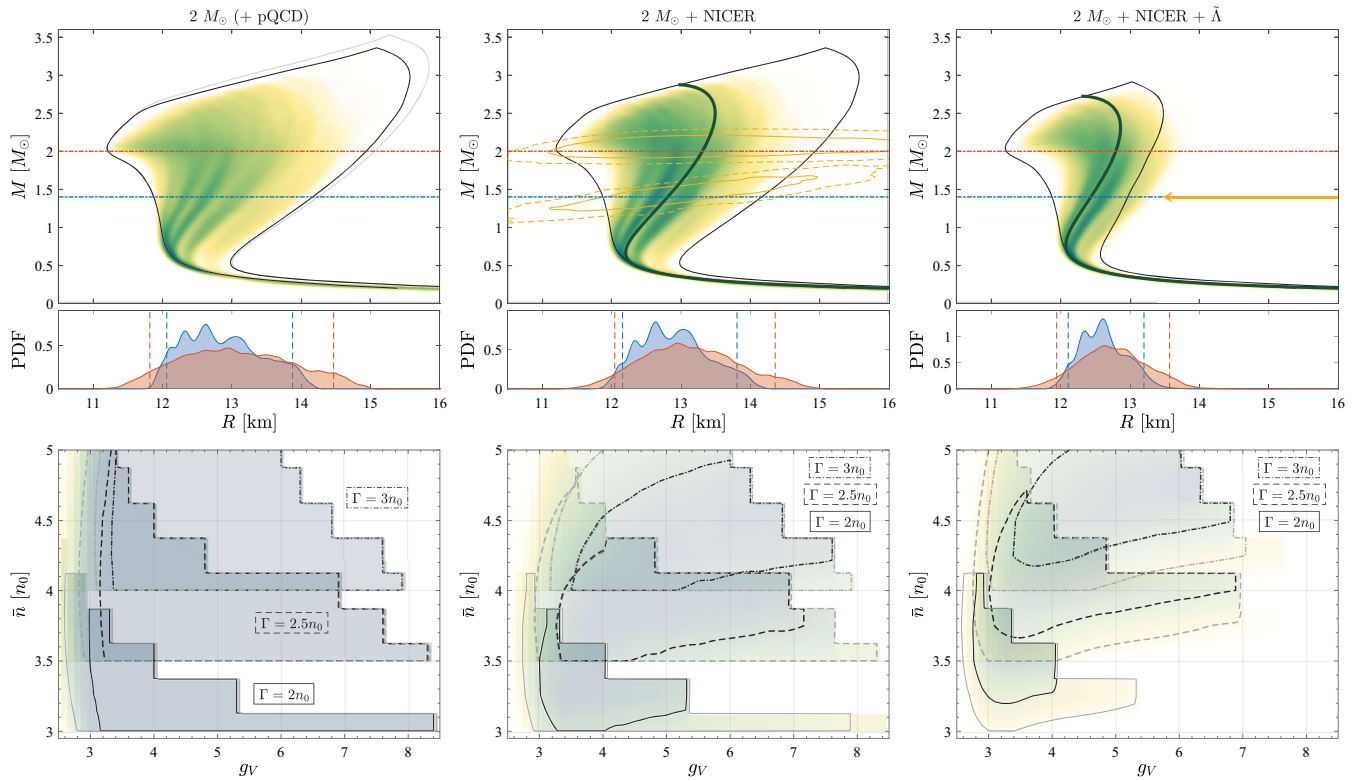
FIG. 3. Posterior probabilities from our Bayesian analysis in the mass-radius plane (top), as well as in different slices of the parameter space (bottom). The probabilities displayed correspond to the SFHo hadronic EOS and $m_\sigma = 290$ MeV, and darker colors indicate higher probabilities. On the mass-radius diagrams, the outer black contours represent the boundaries of all the possible $M - R$ curves using the given constraints. Below the mass-radius diagrams, we show the radius distribution of $1.4M_\odot$ (blue) and $2M_\odot$ (red) NSs, with the 90% confidence intervals indicated by the vertical dashed lines. In the bottom, the posterior probabilities with different measurements in the parameter space are shown in a contour plot, with the two levels indicating the 68% (black) and the 95% (gray) credible intervals, while different contour styles represent different slices in Γ. The three panels side by side correspond to the posterior with the $2M_\odot$ minimal constraint (left), the posterior with the two NICER measurements (middle), and the posterior with the NICER and tidal deformability measurements from GW170817 (right). All panels contain the pQCD minimal constraint as well. On the left, the gray contour represents all $M - R$ curves without the pQCD constraint applied (top), while on the middle and right panels the dark green curves display the maximum posterior probability configurations.

since there is no natural connection between "lengths" in masses and radii. We can sample points along each $M - R$ curve evenly in baryon number density or explicitly define a metric connection between line elements in M and R, etc. Since there is no unique way to introduce this metric, the distribution obtained will be somewhat arbitrary. Hence, the prior distribution in itself will not present definitive information. However, the change between the prior and posterior distributions is independent of the chosen metric and hence portrays faithful information about the posterior probabilities. In our analysis, we choose a metric that suppresses the PDF at low densities and enhances it at high densities, in order to obtain an even distribution of points at all densities.

After taking into account the two NICER measurements (middle panel in Fig. 3) the probabilities are only slightly modified, since, as shown in the top panel, even the one-sigma contours (solid yellow lines) of the two measurements completely overlap with the whole set of $M - R$

diagrams. The EOS parameters for the maximum posterior probability case are $g_V = 6.9$, $\bar{n} = 4n_0$, and $\Gamma = 2.5n_0$. The $M - R$ curve for this parameter set is displayed in the middle panel of Fig. 3.

The change is more drastic when the tidal deformability measurement is taken into account as well. This measurement significantly constrains radii from above (see the indication by the yellow arrow) and consequently reduces the maximally possible NS mass as well to $\max(M_{\max}) < 2.8M_\odot$. In the parameter space, this measurement constrains the value of the vector coupling from above, since large values of g_V would correspond to stiff equations of state, which, in turn, would create NS sequences with large maximum masses and radii. One can observe that the probability density plot in the $M - R$ diagram extends over the black contour to the right. Examining the distribution of $R(1.4M_\odot)$, one can also verify that, while the black contour—corresponding to the 90% bound of $\tilde{\Lambda} < 720$—crosses the $1.4M_\odot$ line at ~ 13 km, the 90%

bound of the radius distribution is ~ 13.2 km. This phenomenon was also reported in, e.g., Ref. [32] and reinforces the necessity of taking the complete data from a given measurement into account instead of simply bounds from some credible intervals. The parameter set corresponding to the maximum probability EOS in this case is $g_V = 6.5$, $\bar{n} = 4.5 n_0$, and $\Gamma = 2.75 n_0$.

In addition to the canonical measurements, we can investigate the constraint imposed by the hypermassive NS hypothesis. Specifically, we can use an upper mass bound based on Ref. [116]. We did not include this measurement in our canonical set, since there is still some ambiguity around the modeling of the kilonova signal AT2017gfo, and therefore the ejected mass in the merger event. The results for this scenario are shown in Fig. 4. The black contour in the top panel that encompasses all the possible $M - R$ curves that meet all the requirements does not shrink at lower masses, which is to be expected for a sufficiently robust ensemble of equations of state. On the other hand, the 90% credible interval for $R(1.4 M_\odot)$ shrinks from a width of 1.10 to 1.04 km and shifts to lower values

from an upper bound of 13.20 to 13.06 km. The main effect of this step on the parameter space, as expected from Sec. III A, is an upper bound on the vector coupling, as can be seen in the lower panel of Fig. 4, which shows the probability densities for $m_\sigma = 290$ MeV. The maximum posterior probability corresponds to the parameter set $g_V = 3.1$, $\bar{n} = 3.5 n_0$, and $\Gamma = 2 n_0$, which means $n_{BU} = 5.5 n_0$. Despite this moderate value, this NS does not develop a quark core.

Alternatively, resolving the hypermassive NS hypothesis, we can keep the BH hypothesis and assume, in addition, that the mass-gap object in GW190814 was an extremely massive NS. Even though, by our current understanding of the nuclear EOS, such a massive NS seems unlikely, it is still allowed by astrophysical measurements, as we show in Fig. 5. Although together with
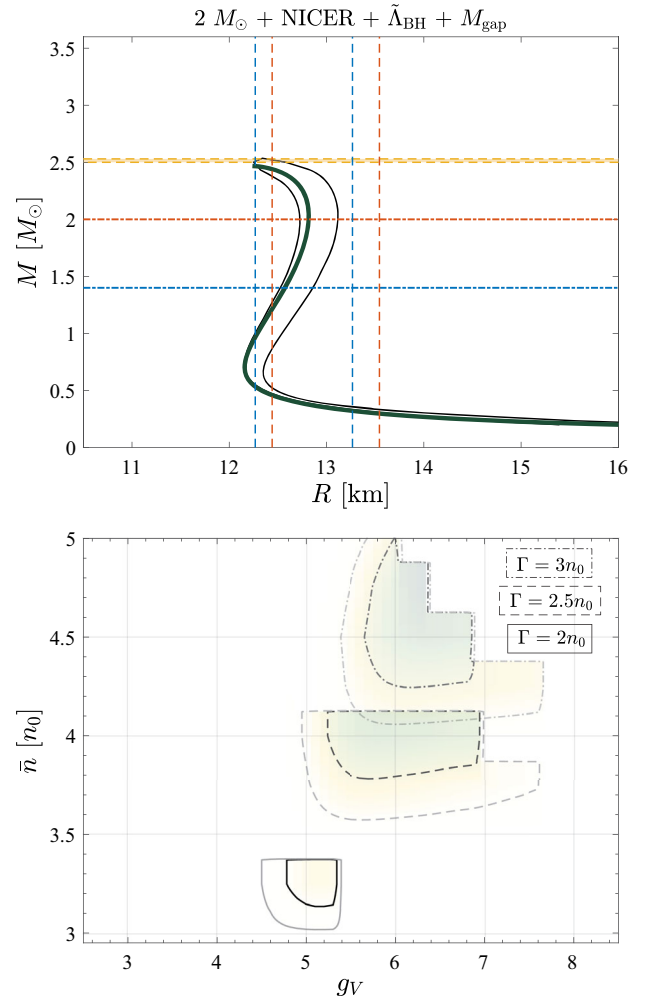
FIG. 5. Same as in Fig. 4, but instead of taking into account the upper mass bound based on the hypermassive NS hypothesis, we only include the constraint from the BH hypothesis, while identifying the mass-gap object in GW190814 as a NS. Because of the statistically low number of equations of state fulfilling these tight constraints, the shapes of the posterior PDFs become irregular, and hence we omit them, only showing the 90% radius bounds.
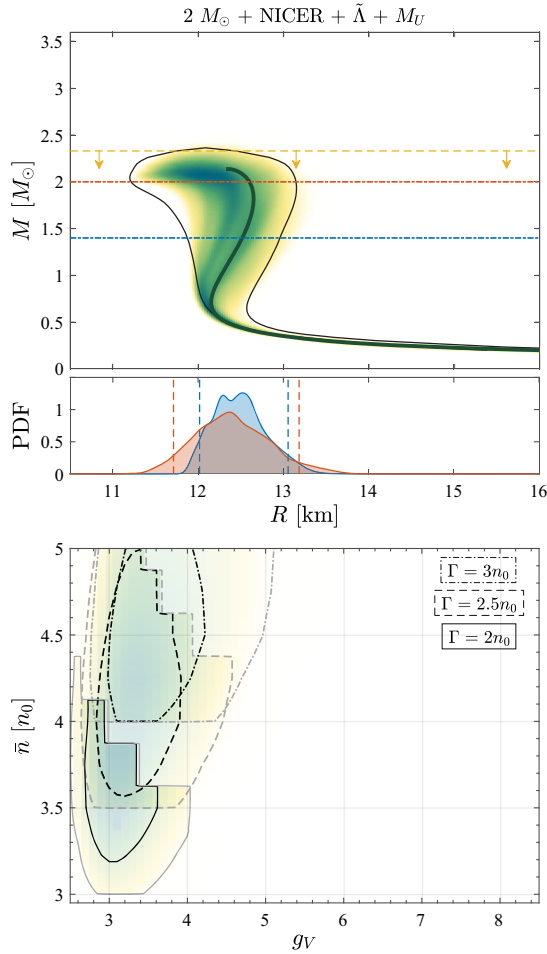

FIG. 4. Same as in Fig. 3, but with the upper mass constraint from the hypermassive NS hypothesis also applied, in addition to the NICER and tidal deformability measurements.

the BH hypothesis they leave only a narrow region for the maximum mass of NS sequences (see the yellow band between $2.5 M_\odot$ and $2.53 M_\odot$). Because of this narrow permitted region, our statistical ensemble of permitted equations of state will be greatly reduced, leaving only ~100 equations of state with sufficiently large posterior probabilities. Therefore, the posterior radius distributions will have an irregular shape and will be unreliable, although the 90% credible intervals might still be used. Note that the difference here between the black contour in the $M - R$ diagram and the 90% credible intervals of the radius distributions is even more pronounced than in the right panel of Fig. 3. The 90% upper bound on $R(1.4 M_\odot)$ here is ~13.3 km, in contrast to the value of ~12.9 km predicted by the black contour. The parameters that correspond to the maximum posterior probability are $g_V = 4.9$, $\bar{n} = 4.25 n_0$, and $\Gamma = 2.75 n_0$.

Finally, Fig. 6 shows the posteriors when, in addition to the NICER and tidal deformability measurements, the BH hypothesis and the constraint from the central compact object inside HESS J1731-347 is also taken into account. The two-sigma credible interval of the measurement barely overlaps with our set of mass-radius curves, however, a considerable region is still allowed on the $M - R$ plane. Comparing the posterior probabilities on the parameter space to those in the bottom right panel in Fig. 3, we see that with this constraint included parameter sets with a low value of $\bar{n}$ are less probable, and the high-probability regions shift to higher values of $\bar{n}$. The maximum posterior probability corresponds to the parameter set $g_V = 4.7$, $\bar{n} = 4.25 n_0$, and $\Gamma = 2.5 n_0$.

We also performed this analysis for different sigma meson masses and the DD2 hadronic EOS as well. Our results for the radius bounds and the highest posterior probability parameter sets can be found in Tables III–VI of Appendix. Radius bounds do not change drastically when using different sigma meson masses, although higher values of m_σ correspond to larger radii. Using the stiffer, DD2 hadronic EOS, on the other hand, results in a significant increase in the radius bounds. In case we set the sigma meson mass to 600 or 700 MeV, we are left with a low number of stable and causal equations of state; therefore, we omitted the analysis for these parameters.

So far we have only investigated the effect of various measurements on the mass-radius diagram and different $g_V - \bar{n}$ slices of the posterior PDFs. It is also instructive to look at different $\bar{n} - \Gamma$ slices and inspect what can be inferred about the parameters of the hadron-quark phase transition. This is shown in Fig. 7, where we calculated the posteriors on a finer grid compared to the previous figures. The two rows correspond to two different slices with a fixed g_V. These two slices were chosen to match the parameters with the maximum posterior probability case in the hypermassive NS hypothesis scenario (top) and the mass-gap NS scenario (bottom). The first three panels in both rows from
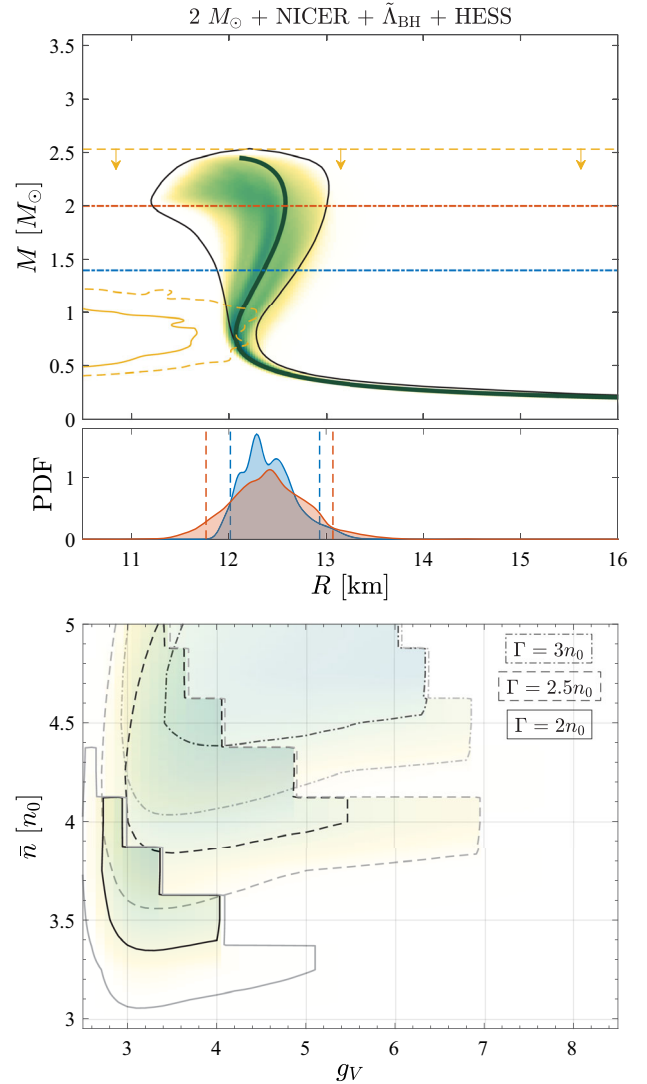

FIG. 6. Same as in Fig. 3, but with the constraint from the central compact object inside HESS J1731-347 also applied, in addition to the NICER and tidal deformability measurements, and the BH hypothesis.

left to right show the posterior with the minimal constraints, the posterior with the NICER measurements, and the posterior with NICER and tidal deformability measurements, respectively. The rightmost panel at the top has the upper mass constraint from the hypermassive NS hypothesis included as well, while the one at the bottom contains the lower mass bound from the mass-gap object and exclusions from the BH hypothesis instead. Hence, these parameter planes can be viewed as an evolution of posterior probabilities with the inclusion of more and more constraints in these two scenarios. The upper left excluded region corresponds to the requirement $\bar{n} - \Gamma \geq n_0$, while the lower right part is excluded due to acausality or instability.

Looking at the top row, at first it might seem like the hypermassive NS hypothesis broadens the region of
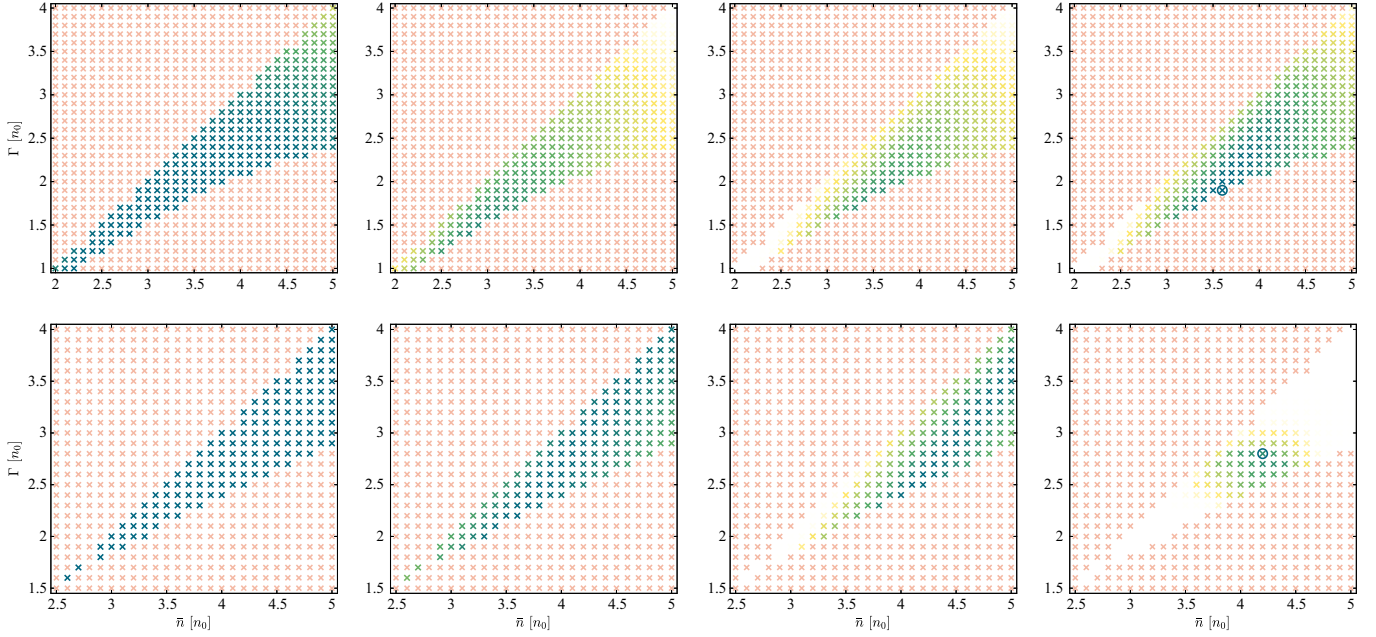
FIG. 7.   Prior and posterior probabilities of different parameter sets in the plane of the phase transition parameters $\bar{n}$ and Γ, for two slices with fixed g_V. Darker colors indicate higher probabilities (white areas correspond to $\sim$0 probability), with probabilities having been normalized by the maximum probability in the complete parameter space (including all g_V). Parameter sets with an orange color are excluded by the requirement $\bar{n} - \Gamma \geq n_0$ or due to acausality and/or instability. The top panels correspond to slices in the parameter space with $g_V = 3.1$, while the bottom panels have $g_V = 4.7$. These values correspond to the equations of state with the maximum posterior probability for the hypermassive NS hypothesis and the mass-gap object scenarios, respectively. The first three panels from left to right both for the top and bottom panels show the posterior with the minimal constraints, the posterior with the NICER measurements, and the posterior with NICER and tidal deformability measurements, respectively. The rightmost panel at the top has the upper mass constraint from the hypermassive NS hypothesis included as well, while the one at the bottom contains instead the BH hypothesis together with the lower mass bound from the mass-gap object in GW190814. Parameter sets with the maximum probability are marked with a ring.

high-probability parameters from the third to the fourth panel. However, this illusion is due to the fact that these probabilities were normalized by the maximum posterior probability of the entire parameter space (including all g_V values); hence probabilities in the second and third panels at the top are suppressed, since the maximum posterior probabilities in these cases correspond to $g_V = 6.9$ (NICER) and $g_V = 6.5$ (NICER + $\tilde{\Lambda}$), respectively, which are outside the parameter space slices shown in Fig. 7. Note, however, that it is not the case for the bottom panels, where the maximum probability case is always closer in g_V to the slice shown. Interestingly, in many cases, higher posterior probabilities are situated close to the edges of the allowed regions, adjacent to unstable or acausal equations of state. This means that the lowest possible value of Γ is preferred for a given $\bar{n}$, which also means that astrophysical observations prefer a very stiff intermediate-density region. Such stiff intermediate regions are also predicted by the theory of the so-called quarkyonic matter (see, e.g., Refs. [33,34]). The two scenarios depicted in Fig. 7 end up with different preferred values for $\bar{n}$ and Γ, and the preferred value of these parameters also varies from step to step; hence no robust statement can be made about the

values of the phase transition parameters. However, very low values of $\bar{n}$ and Γ are disfavored after taking into account the tidal deformability measurement, hence the existence of pure quark matter at densities below $\sim 4 n_0$ is also disfavored.

2. Results for the complete EOS ensemble

After performing the analysis for the restricted case, we repeat it with our complete EOS ensemble in order to get more representative results for the radius bounds, the preferred parameters, and also generally for bounds on the EOS itself. Figure 8 yet again shows the posterior PDFs on the mass-radius plane and for the radii of $1.4 M_\odot$ and $2 M_\odot$ NSs. We also show the contours as a result of sharp cutoffs separately for the SFHo (solid contour) and the DD2 (dashed contour) hadronic equations of state, since at low densities the two hadronic equations of state produce very different radii. Additionally, we also show the regions where, given the specific constraints, hybrid stars with pure quark cores can exist. For this analysis, we define matter being in pure quark state when the density is above $n_B > n_{BU} = \bar{n} + \Gamma$, hence the EOS is characterized by our quark model.
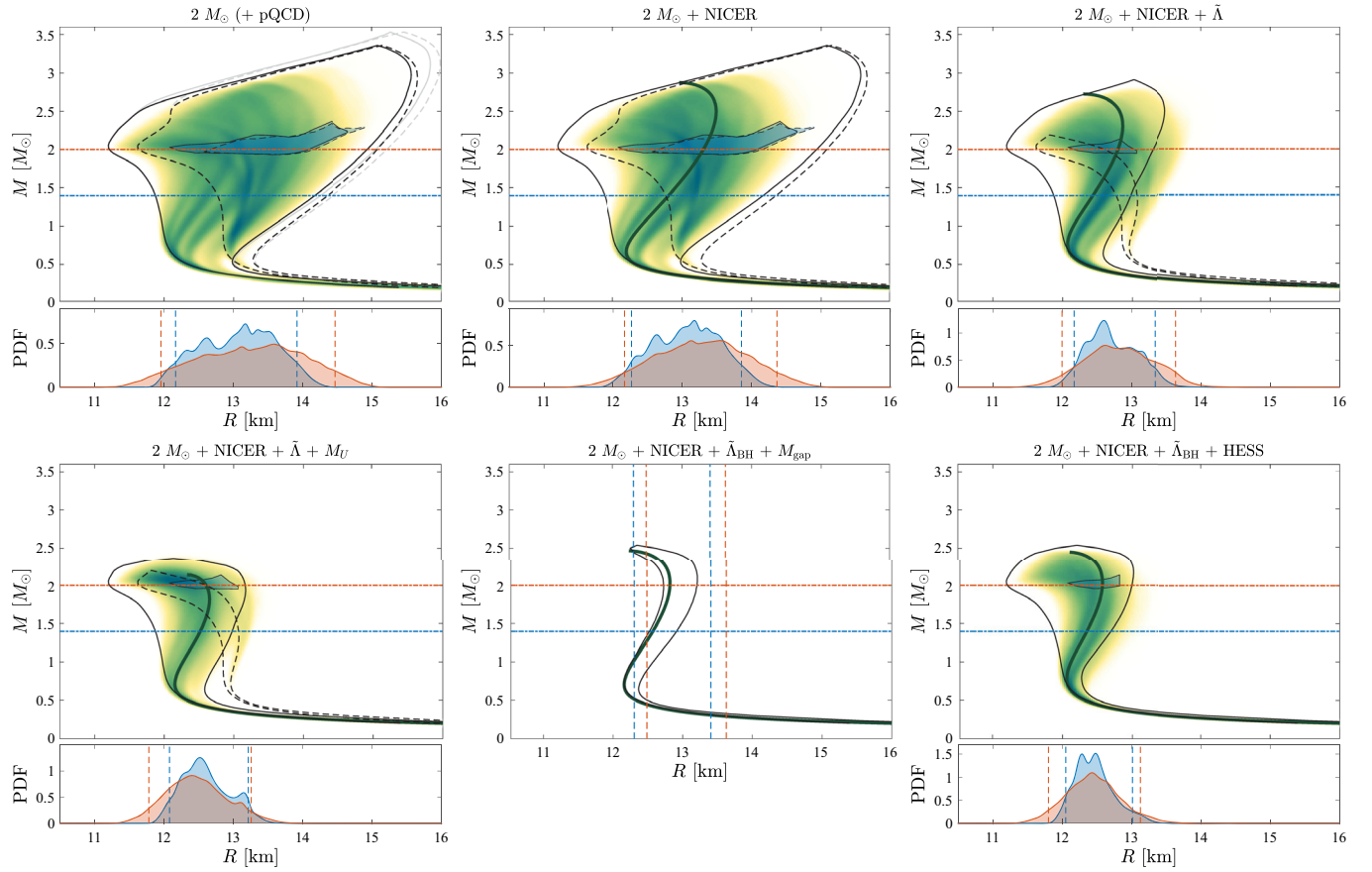
FIG. 8. Posterior probabilities from our Bayesian analysis in the mass-radius plane, using the complete set of equations of state with different sigma meson masses, and the SFHo and DD2 hadronic equations of state combined. Darker colors indicate higher probabilities. The outer black contours represent the boundaries of all the possible $M - R$ curves using the given constraints for the SFHo (solid) and the DD2 (dashed) hadronic equations of state. The radius distribution of $1.4M_\odot$ (blue) and $2M_\odot$ (red) NSs is also shown, with the 90% confidence intervals indicated by the vertical dashed lines. The measurements taken into account for each panel are indicated above them. The pQCD minimal constraint is included in every panel. On the left, the gray contour represents all $M - R$ curves without the pQCD constraint applied (top), while on the middle and right panels the dark green curves display the maximum posterior probability configurations. The inner blue regions on the $M - R$ diagrams represent NSs with pure quark cores. In the mass-gap object scenario, due to the statistically low number of equations of state fulfilling the tight constraints, the shapes of the posterior PDFs become irregular, and hence we do not show them, only the 90% radius bounds.

An interesting feature of the region of NSs with a pure quark core is that there is an upper mass bound for these objects ($\sim 2.35 M_\odot$), which might not seem obvious at first. However, one can understand this by examining the sound speed squared in the intermediate-density region (at ~ 3–$5 n_0$, see, e.g., Fig. 10 in Ref. [88]). First, there is a stiff peak that is then followed by a valley, which, in some cases, can get close to $c_s^2 \approx 0$. After this valley, the sound speed increases and only then the quark EOS is reached. Therefore, equations of state that exhibit a large peak in the beginning and hence create high-mass NSs have a huge drop in the speed of sound, which makes these NS sequences prone to becoming unstable before they can develop a pure quark core. Interestingly, Ref. [29] finds a similar upper mass bound for NSs with pure quark cores ($\sim 2.25 M_\odot$) using a completely different definition for a pure quark core.

Because of the stiffness of the DD2 hadronic EOS, upper bounds on radii constrain mass-radius curves with the DD2 EOS even more. The tidal deformability constraint limits the maximum possible NS mass more significantly than in the case of the SFHo hadronic EOS, to $\max(M_{\max}) < 2.2 M_\odot$. The region of hybrid stars with a pure quark core also shrinks significantly for the SFHo EOS, and it even disappears for the DD2 EOS in this case. Adding the hypermassive NS hypothesis to this measurement does not constrain $M - R$ curves with the DD2 EOS any further, neither does it reduce the region of hybrid stars with a quark core for $M - R$ curves with the SFHo EOS. For the mass-gap object scenario, interestingly, equations of state created by using the relatively stiff DD2 EOS for the hadronic part cannot produce any $M - R$ curves that can satisfy the conditions $\tilde{\Lambda} < 720$ and $M_{\max} > 2.5 M_\odot$ at the same time.
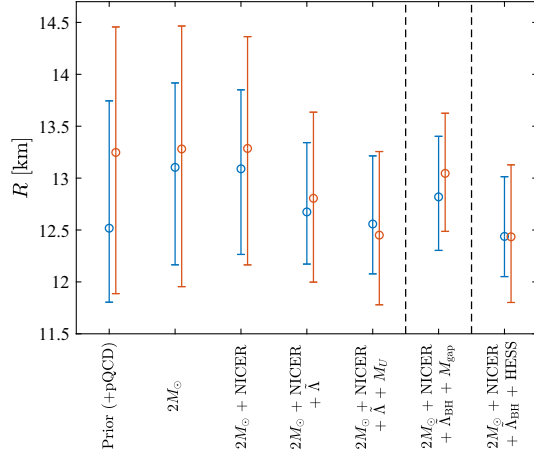
FIG. 9. Radius intervals for $1.4 M_\odot$ (blue) and $2 M_\odot$ (red) NSs. The circles represent the median values, while error bars correspond to the 90% credible intervals. The vertical dashed lines separate alternative scenarios and additional recent measurements. Data for these intervals can be found in Table I.

TABLE I. Median values of radii for $1.4 M_\odot$ and $2 M_\odot$ NSs for the different astrophysical constraints investigated in this paper. The errors represent the 90% credible intervals. The pQCD minimal constraint is included in each case.

Measurement	$R_{1.4}$ (km)	$R_{2.0}$ (km)
Prior (+pQCD)	$12.52^{+1.23}_{-0.71}$	$13.25^{+1.21}_{-1.36}$
$2M_\odot$	$13.10^{+0.81}_{-0.94}$	$13.28^{+1.18}_{-1.33}$
$2M_\odot$ + NICER	$13.09^{+0.76}_{-0.82}$	$13.29^{+1.08}_{-1.12}$
$2M_\odot$ + NICER + $\tilde{\Lambda}$	$12.67^{+0.67}_{-0.50}$	$12.81^{+0.83}_{-0.81}$
$2M_\odot$ + NICER + $\tilde{\Lambda}$ + M_U	$12.56^{+0.66}_{-0.48}$	$12.45^{+0.81}_{-0.67}$
$2M_\odot$ + NICER + $\tilde{\Lambda}_{BH}$ + M_{gap}	$12.82^{+0.58}_{-0.52}$	$13.05^{+0.58}_{-0.56}$
$2M_\odot$ + NICER + $\tilde{\Lambda}_{BH}$ + HESS	$12.44^{+0.58}_{-0.39}$	$12.43^{+0.69}_{-0.63}$

TABLE II. Parameter sets corresponding to equations of state with the maximum posterior probability for various measurements. m_σ is given in MeV, while $\bar{n}$ and Γ are given in units of the saturation density n_0.

	ϑ_{max}
Measurement	EOS, m_σ, g_V, $\bar{n}$, Γ
$2M_\odot$ + NICER	SFHo, 290, 6.9, 4, 2.5
$2M_\odot$ + NICER + $\tilde{\Lambda}$	SFHo, 290, 6.5, 4.5, 2.75
$2M_\odot$ + NICER + $\tilde{\Lambda}$ + M_U	SFHo, 290, 3.1, 3.5, 2
$2M_\odot$ + NICER + $\tilde{\Lambda}_{BH}$ + M_{gap}	SFHo, 290, 4.9, 4.25, 2.75
$2M_\odot$ + NICER + $\tilde{\Lambda}_{BH}$ + HESS	SFHo, 290, 4.7, 4.25, 2.5

This is due to the fact that the first of these two conditions limits radii of low-mass NSs from above and since a stiff hadronic EOS generates larger radii, in general, this condition will limit the maximum mass of NSs (as can be seen in the top right panel of Fig. 8). Therefore, the existence of very massive NSs is only possible in case the hadronic EOS is soft enough to produce sufficiently small radii. Another interesting consequence of the mass-gap object interpreted as a NS is that none of the NSs would have a core consisting of pure quark matter in this case. This can be understood by noting that the maximum mass of such hybrid stars is $\sim 2.35 M_\odot$, while the minimum required mass for maximally stable NSs is higher in this case. Considering the measurement from the central object of HESS J1731-347, none of the NSs with the DD2 EOS is allowed, since they generally predict large radii for low-mass NSs.

We summarize our results for the calculated posterior radius distributions of $1.4 M_\odot$ and $2 M_\odot$ NSs for various astrophysical constraints in Table I and Fig. 9. Note, however, that these results should be taken with a grain of salt, since our prior was not preprocessed in order to acquire a uniform radius prior, which should be done in order to obtain meaningful results (see, e.g., Ref. [114]). Note also, that although it is not mentioned in Table I and Fig. 9 explicitly, our prior includes constraints from our constituent quark model implicitly, which restrict radii to values $R_{1.4} \gtrsim 12$ km. The parameter sets corresponding to the maximum posterior probabilities for different sets of measurements are summarized in Table II. Interestingly, all of the maximum posterior probability equations of state have $m_\sigma = 290$ MeV and the SFHo EOS for the hadronic part.

The prior and posterior marginalized one- and two-dimensional PDFs of the model parameters can be found in

Fig. 13 in the Appendix. Looking at the prior, we can see that there are very few stable and causal configurations for $m_\sigma = 600$ MeV and there are almost none for $m_\sigma = 700$ MeV. Even though the maximum posterior probabilities always correspond to $m_\sigma = 290$ MeV, equations of state with higher sigma meson masses are not suppressed, and they are even enhanced for the hypermassive NS hypothesis scenario.

We also study the amount of quark matter contained in hybrid stars that have a quark core. We identify a NS core being made out of quark matter in case the baryon density rises above $n_{BU} = \bar{n} + \Gamma$. In addition to this condition, we also require the chiral phase transition to have occurred at that density. We define this by requiring the nonstrange scalar condensate in our constituent quark model to drop below 10% of its vacuum value. Even though this seems like an overly strict definition, this only excludes a few percent of NSs that would have a quark core by the first requirement only. In Fig. 10, we show the amount of quark matter contained in hybrid stars that develop such a quark core. Here, no additional constraints were added on top of the minimal ones ($2 M_\odot$ and pQCD constraints). In many cases the quark core is light with masses of $M_{quark} < 0.05 M_\odot$. However, some hybrid stars can develop
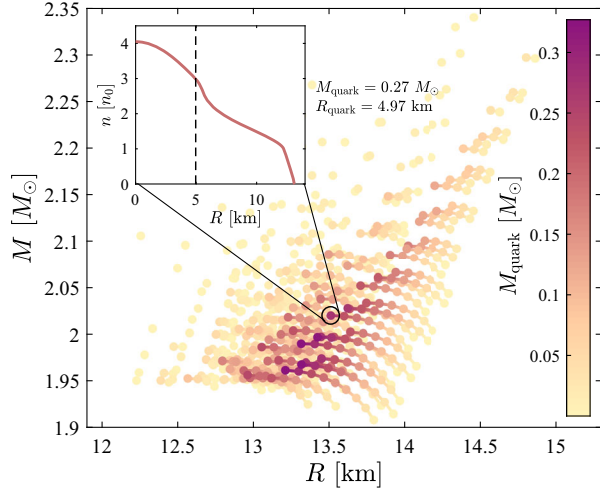
FIG. 10. Masses of quark cores for hybrid stars that develop such a core. The inset shows the radial dependence of the baryon density inside one of the hybrid stars that have a sizable quark core. The vertical dashed line represents the boundary between the quark core and the outer layers.

a sizable quark core, with radii $R_{\text{quark}} \gtrsim 5$ km (see the inset in Fig. 10). More massive cores correspond to NS sequences with lower maximum masses with the most massive core having a mass $M_{\text{quark}} \approx 0.33 M_\odot$. This corresponds to a NS with a mass of $1.96 M_\odot$. A similar figure can be found in Ref. [29] about the radii of quark cores in $2 M_\odot$ NSs.

Combining the complete ensemble of our equations of state, we can investigate the effect of various constraints on the EOS itself. The left panel of Fig. 11 shows the 90% credible intervals of the sound speed squared as a function of energy density for various astrophysical constraints. The prior in itself exhibits a peak in the sound speed, which is located at $\varepsilon \approx 400$ MeV/fm^3 for the lower bound. This can

be attributed to the eLSM and the concatenation between the hadronic and quark equations of state. This peak translates to the lack of NSs with small radii in the $M-R$ plane in Fig. 3. However, this lower bound is slightly increased when we include the $2M_\odot$, as well as the NICER and tidal deformability measurements. This may be the result of the $2M_\odot$ constraint, which requires a minimal stiffness for the equations of state, and also the NICER measurements, which disfavor small radii. The effect of the tidal deformability measurement of GW170817 is the reduction of the upper bound for energy densities $\varepsilon \lesssim 500$ MeV/fm^3, which reduces the radii of $1.4M_\odot$ NSs.

In the middle panel of Fig. 11 we compare the two alternative scenarios with the hypermassive NS hypothesis and the mass-gap NS included, respectively. With the upper mass bound from the hypermassive NS hypothesis included in addition to the previous measurements, the upper bound of the sound speed squared is reduced from ~ 0.8 to ~ 0.6. The effect of astrophysical constraints on the upper bound above $\varepsilon \gtrsim 1200$ MeV/fm^3 is minor, while it is negligible for the lower bound. In both cases, an intermediate-density peak in the sound speed squared is preferred. The position of this peak is similar in the two cases, with $\varepsilon_{\text{p}} = 565^{+71}_{-102}$ MeV/fm^3 for the hypermassive NS and $\varepsilon_{\text{p}} = 580^{+57}_{-83}$ MeV/fm^3 for the mass-gap NS scenario. The values of the peaks are $0.48^{+0.08}_{-0.06}$ and $0.64^{+0.07}_{-0.07}$, respectively. These numbers correspond to medians and 68% credible intervals. We note that Ref. [30] arrives at a similar result for the position of the peak in an independent analysis, however, their median value of the peak is higher than ours. The energy density reached in the center of the maximally stable NSs in the two cases are $\varepsilon_{\text{max}} = 1089^{+93}_{-121}$ and $\varepsilon_{\text{max}} = 1008^{+63}_{-71}$ MeV/fm^3, respectively, while for the baryon densities these values are $n_{B,\text{max}} = 0.89^{+0.07}_{-0.08}$ and $n_{B,\text{max}} = 0.80^{+0.04}_{-0.05}$ fm^{-3}. Note that the maximum energy
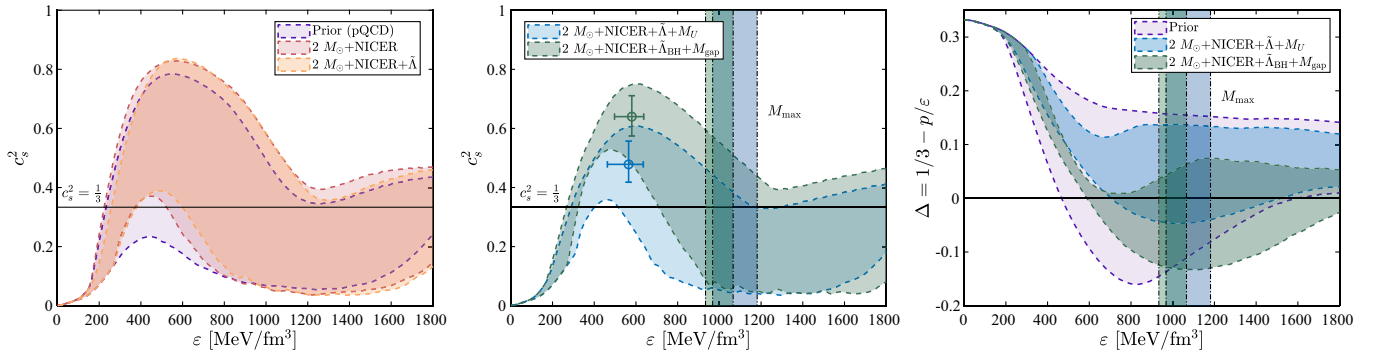

FIG. 11. The 90% credible intervals of the sound speed squared (left and middle) and the trace anomaly (right) as a function of energy density under various constraints, using the full ensemble of our equations of state. Different contours show results for the prior with the pQCD constraint (purple), the posterior with the NICER (red), and the NICER and tidal deformability measurements (yellow). In the middle, the posteriors for the hypermassive NS hypothesis (blue) and for the alternative scenario where the mass-gap object in GW190814 is considered a NS (green) are shown. The position of the speed of sound peaks (circles in the middle panel) with the 68% credible intervals denoted by the error bars and the energy density at the center of maximally stable NSs (vertical lines in the middle and right panels, similarly with the 68% credible intervals) is also displayed.

density and baryon density is lower for the mass-gap NS case, in which the maximally massive NSs have larger masses. This follows from the fact that a larger peak in the speed of sound, which creates heavier NSs, will lead to an earlier destabilization after the speed of sound drops to reach the pQCD limit at high densities.

One can interpret the peak in the speed of sound as a dominance of repulsive interactions, as opposed to the finite temperature case, where it never exceeds the conformal limit [74,139,140]. This might be interpreted as an indication of deconfinement, which might be linked to the percolation of hadrons. Using a simple model one can estimate the density at which percolation occurs (see, e.g., Ref. [30]). In Ref. [30] the authors use an average mass radius of protons of $r_p = (0.80 \pm 0.05)$ fm (taken from Ref. [141]) that is directly extracted from experimental data of ϕ meson photoproduction, yielding a density of $n_{\rm B,p} = 0.57^{+0.12}_{-0.09}$ fm^{-3}. This density is obtained from percolation theory through the expression $n_{\rm B,p} = 1.22/V_0$, where $V_0 = 4r_p^3 \pi/3$ [142,143]. Reference [30] arrives at a value $n_{\rm B,p} = 0.56^{+0.09}_{-0.08}$ fm^{-3}, which is remarkably close to the estimated value of the percolation density. For the hypermassive NS and the mass-gap NS scenarios, we calculate the density of the peak to be at $0.53^{+0.06}_{-0.08}$ and $0.53^{+0.04}_{-0.06}$ fm^{-3}, respectively, which are slightly lower but still consistent with the estimated density of percolation. It is worth noting that for the mass radius of proton there are several competing results on the market starting from as low as $r_p = (0.55 \pm 0.03)$ fm [144] up to $r_p = (0.86 \pm 0.08)$ [145]. Moreover, beside the mass radius of protons there is also the charge radius of protons, which can be measured accurately by electron scattering experiments. Currently, there are two competing, nonoverlapping values of $r_{\rm Ep} = 0.84$ and 0.88 fm [146–148]. Thus, the size of the proton is still under debate and can be as low as 0.55 fm, which would give a much higher percolation density. Also note that the peak in the speed of sound might be a feature of the quark model itself, in case that the phase transition occurs at lower densities. Reference [63] finds that a low onset of the phase transition and a color superconducting quark model is consistent with the speed of sound peak from astrophysical data.

In the right panel of Fig. 11, we also show the limits for the trace anomaly, defined as

$$\Delta = \frac{1}{3} - \frac{p}{\varepsilon}. \tag{25}$$

This was recently proposed as a measure of conformality [149]. As we approach the conformal limit, the value of Δ will tend to zero. Similar to the results of Ref. [30], we find that the value of Δ approaches zero from above in the hypermassive NS scenario for large ε values. This is to be compared to the mass-gap NS scenario, where the

conformal limit can be reached both from above and below; in fact, quite remarkably, at $\varepsilon \approx 800$ MeV/fm^3 a negative value for Δ becomes highly favored.

Yet another recent study [70] proposes another quantity to measure conformality. They combine the trace anomaly with its logarithmic derivative and define d_c as

$$d_c = \sqrt{\Delta^2 + \Delta'^2}, \tag{26}$$

where

$$\Delta' = \frac{d\Delta}{d\ln\varepsilon} = c_s^2\left(\frac{1}{\gamma} - 1\right), \tag{27}$$

with $\gamma = d\ln p/d\ln\varepsilon$ being the polytropic index. Based on the observation that hadronic equations of state can be
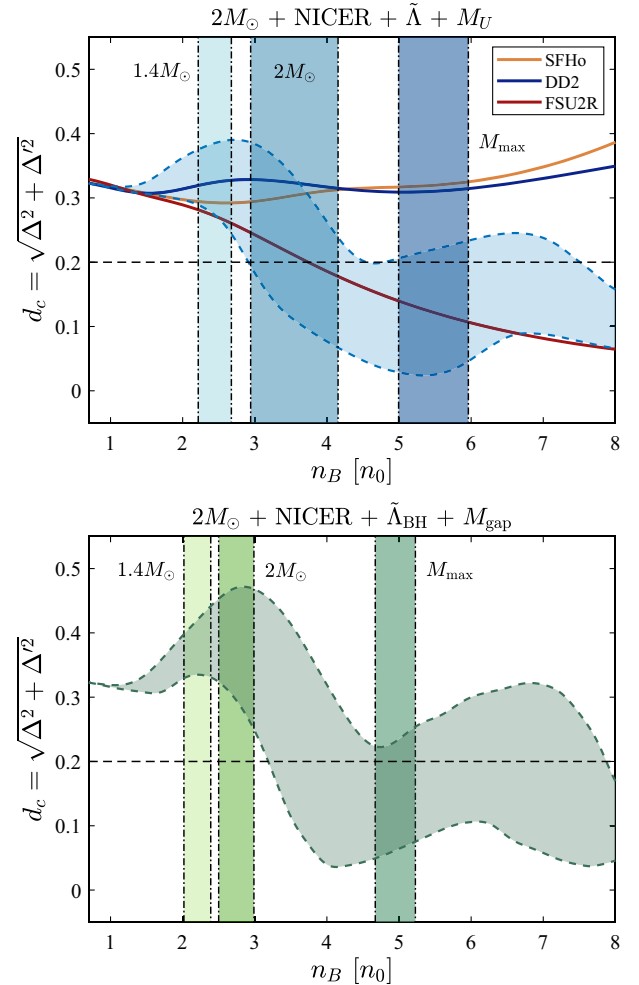

FIG. 12. 90% credible intervals for the measure of conformality d_c, as a function of baryon density, for the hypermassive NS scenario (top) and the mass-gap object scenario (bottom) using the full ensemble of our EOS. Vertical ares denote the 90% intervals for the central densities of $1.4M_\odot$, $2M_\odot$, and maximally stable NSs, with increasingly dark colors. Solid lines show the density dependence of d_c for hadronic equations of state.

separated from conformal systems using this quantity and that for a first-order phase transition d_c is bounded from below by $d_c \gtrsim 0.236$ at the phase transition, they propose that conformal matter can be identified by the criterion $d_c < 0.2$. We should add, however, that some hadronic equations of state do not comply with this conjecture. For example, in Fig. 12 we show the density dependence of d_c for the FSU2R EOS [150] downloaded from the CompOSE database. This is a purely nucleonic EOS containing an ω^4 interaction term, and yet it behaves similar to hybrid equations of state, with $d_c < 0.2$ for $n_B > 4n_0$. Therefore, this criterion of conformality should be further studied.

We investigate this measure in Fig. 12 for the two alternative scenarios with the hypermassive NS hypothesis and the mass-gap object identified as a NS. In both cases, d_c drops below 0.2 before reaching the density at the center of maximally stable NSs. However, for the hypermassive NS scenario, this happens at lower densities, at around $3 - 4n_0$, while for the mass-gap object scenario, this interval is at ~ 3.5–$4.5n_0$. Interestingly, for the hypermassive NS scenario, NSs with $\sim 2M_\odot$ might already possess conformal matter, while for the other case, matter inside $2M_\odot$ NSs is far from being conformal.

IV. CONCLUSION

In this paper, we have investigated what can be inferred from astrophysical observations about the properties of quark matter inside NSs and the phase transition between the hadronic and quark phases. For this purpose, we have utilized the (axial) vector meson extended linear sigma-model to describe quark matter at high densities, the SFHo and DD2 models as hadronic equations of state representing soft and stiff hadronic models, respectively. To transition from the hadronic to the quark model, we have used a general polynomial concatenation, the parameters of which can be varied to create phase transitions at different densities. The whole parameter space with four parameters (two from the concatenation and two from the constituent quark model) was studied by applying the full PDFs from recent astrophysical observations.

First of all, we have shown that there is a tight correlation between the parameters of the constituent quark model and the maximum mass attainable by heavy NSs described by that model, even though many of the maximum mass NSs do not have pure quark matter in their cores. Hence, some properties of quark matter at high densities might be inferred by only gaining information about the intermediate-density region, and therefore determining the maximum mass of NSs might be used to deduce information about the properties of strongly interacting matter at high densities.

In our Bayesian analysis, we have investigated the effect of different astrophysical measurements on mass-radius curves, the radius distribution of NSs with specific masses, and on the posterior probabilities of different parameter sets. In addition to the lower mass limit from $2M_\odot$ stars and constraints from pQCD, we have also considered the two NICER measurements and the tidal deformability data obtained from GW170817. Moreover, we have studied the effect of additional constraints, such as the upper mass bound inferred from the hypermassive NS hypothesis, interpreting the mass-gap object in GW190814 as a very massive NS, or the mass-radius data obtained from the light compact object in HESS J1731-34. We divided our analysis into two parts. First, we investigated the results in a reduced parameter space with $m_\sigma = 290$ MeV and the SFHo hadronic EOS. We also calculated the results for reduced parameter spaces with other parameters. Then, we combined the full ensemble of ~ 18000 equations of state to deduce more general conclusions about the EOS of strongly interacting matter.

We have shown that the 90% credible regions on the mass-radius diagram obtained by using the complete observational data of GW170817 differ slightly from those originating from a sharp cutoff using the 90% bound on the parameters of the binary corresponding to GW170817. This was also discussed in Ref. [32] and suggests the use of the full PDFs from astrophysical measurements for more precise predictions.

We have also found that the maximum mass of hybrid stars with a pure quark core is below $< 2.35M_\odot$. This is caused by the fact that there is a successive stiffening and softening in the intermediate-density region of our equations of state and in order to reach the density of our quark model, the NS sequence needs to go through the soft region without becoming unstable. Interestingly, Ref. [29] finds a similar upper bound for such hybrid stars in a completely independent analysis. Further constraints narrow down this region even more, leaving only a small space for hybrid stars, with a pure quark core for equations of state, with a soft hadronic part, and none for ones with a stiff hadronic part. This is also in line with the findings of some other studies [123,151–153], which also suggest the possible existence of pure quark matter inside massive NSs, although in a restricted parameter region, highly dependent on the hadronic EOS.

Additionally, we have also shown how the parameters of the hadron-quark concatenation are affected by the various astrophysical constraints. For the two main scenarios considered in this paper, we have found that the parameter encoding the central density of the phase is above $\bar{n} > 3n_0$, and that the appearance of pure quark matter at densities below $\sim 4n_0$ is disfavored in both scenarios, using our parametrization.

Even though the presence of pure quark matter is restricted to a limited region in the mass-radius diagram, we find that a peak in the speed of sound is preferred by astrophysical observations, which might be interpreted as a consequence of reaching percolation densities. We have found that this peak is at $\varepsilon_{\mathrm{p}} = 565^{+71}_{-102}$ and

580^{+57}_{-83} MeV/fm^3 for the hypermassive NS and the mass-gap NS cases, respectively, or at $n_{B,p} = 0.53^{+0.06}_{-0.08}$ and $0.53^{+0.04}_{-0.06}$ fm^{-3}, regarding baryon densities. This is consistent with the findings of Ref. [30] and the prediction of simple percolation models. Reference [69] also reports a value of $\sim 3.3n_0$ for the location of the peak. We have also shown the dependence of the Δ trace anomaly on the energy density and found that in the mass-gap NS scenario a negative Δ is preferred at some energy density region. Additionally, we have investigated the baryon density dependence of d_c, proposed as another measure of conformality by Ref. [70] and have found that the conformal region is reached in the centers of massive NSs for both scenarios. We have also found that in the hypermassive NS scenario, the conformal region can be already reached by $2M_\odot$ NSs.

Equations of state used in this paper can be found in Ref. [81].

ACKNOWLEDGMENTS

APPENDIX: TABLES AND FIGURE

This section contains tables for the radius bounds of $1.4M_\odot$ and $2M_\odot$ NSs, as well as for the parameter sets corresponding to the maximum posterior probability cases, using different sets of equations of state with specific values for the sigma meson mass and the hadronic EOS. We also included a figure about marginalized prior and posterior PDFs in the parameter space of our model, for different astrophysical measurements.

TABLE III. Median and 90% bounds for the radii of $1.4M_\odot$ and $2M_\odot$ NSs using the SFHo hadronic EOS and various values for the sigma meson masses. Results are shown for different combinations of astrophysical measurements. Results for $m_\sigma = 600$ and $m_\sigma = 700$ MeV were omitted due to the low statistics of stable and causal equations of state with these parameters.

Measurement	$m_\sigma = 290$ MeV		$m_\sigma = 400$ MeV		$m_\sigma = 500$ MeV	
	$R_{1.4}$ (km)	$R_{2.0}$ (km)	$R_{1.4}$ (km)	$R_{2.0}$ (km)	$R_{1.4}$ (km)	$R_{2.0}$ (km)
Prior (+pQCD)	$12.13^{+1.49}_{-0.40}$	$13.00^{+1.46}_{-1.25}$	$12.35^{+1.29}_{-0.52}$	$13.06^{+1.30}_{-1.22}$	$12.69^{+0.94}_{-0.70}$	$13.16^{+1.09}_{-1.22}$
$2M_\odot$	$12.82^{+1.05}_{-0.76}$	$13.02^{+1.44}_{-1.21}$	$12.91^{+0.90}_{-0.76}$	$13.09^{+1.28}_{-1.19}$	$13.01^{+0.71}_{-0.68}$	$13.20^{+1.07}_{-1.27}$
$2M_\odot$ + NICER	$12.88^{+0.93}_{-0.72}$	$13.09^{+1.26}_{-1.05}$	$12.94^{+0.82}_{-0.69}$	$13.14^{+1.15}_{-1.03}$	$13.03^{+0.67}_{-0.60}$	$13.23^{+0.98}_{-1.01}$
$2M_\odot$ + NICER + $\tilde{\Lambda}$	$12.59^{+0.61}_{-0.49}$	$12.73^{+0.84}_{-0.79}$	$12.63^{+0.59}_{-0.45}$	$12.75^{+0.82}_{-0.76}$	$12.76^{+0.52}_{-0.43}$	$12.85^{+0.74}_{-0.79}$
$2M_\odot$ + NICER + $\tilde{\Lambda}$ + M_U	$12.47^{+0.59}_{-0.45}$	$12.38^{+0.81}_{-0.67}$	$12.51^{+0.57}_{-0.42}$	$12.42^{+0.79}_{-0.64}$	$12.61^{+0.53}_{-0.37}$	$12.44^{+0.74}_{-0.58}$
$2M_\odot$ + NICER + $\tilde{\Lambda}_{BH}$ + M_{gap}	$12.70^{+0.57}_{-0.43}$	$12.95^{+0.59}_{-0.51}$	$12.78^{+0.54}_{-0.47}$	$12.98^{+0.58}_{-0.50}$	$12.86^{+0.48}_{-0.38}$	$13.10^{+0.52}_{-0.43}$
$2M_\odot$ + NICER + $\tilde{\Lambda}_{BH}$ + HESS	$12.38^{+0.56}_{-0.36}$	$12.40^{+0.67}_{-0.64}$	$12.44^{+0.52}_{-0.37}$	$12.44^{+0.68}_{-0.62}$	$12.57^{+0.52}_{-0.33}$	$12.51^{+0.66}_{-0.62}$

TABLE IV. Median and 90% bounds for the radii of $1.4M_\odot$ and $2M_\odot$ NSs using the DD2 hadronic EOS and various values for the sigma meson masses. Results are shown for different combinations of astrophysical measurements. Results for $m_\sigma = 600$ MeV and $m_\sigma = 700$ and for some combinations of astrophysical measurements were omitted due to the low statistics of stable and causal equations of state with these parameters.

Measurement	$m_\sigma = 290$ MeV		$m_\sigma = 400$ MeV		$m_\sigma = 500$ MeV	
	$R_{1.4}$ (km)	$R_{2.0}$ (km)	$R_{1.4}$ (km)	$R_{2.0}$ (km)	$R_{1.4}$ (km)	$R_{2.0}$ (km)
Prior (+pQCD)	$13.14^{+0.89}_{-1.05}$	$13.70^{+1.05}_{-1.17}$	$13.16^{+0.82}_{-0.61}$	$13.67^{+0.96}_{-1.14}$	$13.23^{+0.69}_{-0.45}$	$13.58^{+0.93}_{-1.11}$
$2M_\odot$	$13.48^{+0.69}_{-0.39}$	$13.72^{+1.04}_{-1.10}$	$13.47^{+0.62}_{-0.38}$	$13.69^{+0.95}_{-1.08}$	$13.43^{+0.57}_{-0.37}$	$13.60^{+0.92}_{-1.05}$
$2M_\odot$ + NICER	$13.44^{+0.65}_{-0.33}$	$13.67^{+0.96}_{-0.93}$	$13.44^{+0.59}_{-0.33}$	$13.65^{+0.90}_{-0.92}$	$13.43^{+0.53}_{-0.33}$	$13.60^{+0.84}_{-0.92}$
$2M_\odot$ + NICER + $\tilde{\Lambda}$	$13.26^{+0.29}_{-0.22}$	$13.30^{+0.56}_{-0.80}$	$13.27^{+0.29}_{-0.22}$	$13.29^{+0.55}_{-0.78}$	$13.26^{+0.29}_{-0.22}$	$13.23^{+0.58}_{-0.74}$
$2M_\odot$ + NICER + $\tilde{\Lambda}$ + M_U	$13.17^{+0.27}_{-0.20}$	$12.95^{+0.58}_{-0.71}$	$13.17^{+0.27}_{-0.19}$	$12.98^{+0.55}_{-0.69}$	$13.17^{+0.26}_{-0.17}$	$12.91^{+0.50}_{-0.59}$

TABLE V. Parameters of equations of state with the maximum posterior probability for different combinations of astrophysical measurements, using the SFHo hadronic EOS. Results for $m_\sigma = 600$ MeV and $m_\sigma = 700$ MeV were omitted due to the low statistics of stable and causal equations of state with these parameters.

Measurement	$\vartheta_{\max}$: $(g_V, \bar{n}\ [n_0], \Gamma\ [n_0])$		
	$m_\sigma = 290$ MeV	$m_\sigma = 400$ MeV	$m_\sigma = 500$ MeV
$2M_\odot$ + NICER	6.9, 4, 2.5	6.3, 5, 3.75	6, 5, 3.75
$2M_\odot$ + NICER + $\tilde{\Lambda}$	6.5, 4.5, 2.75	5.4, 5, 3.5	5, 5, 3.5
$2M_\odot$ + NICER + $\tilde{\Lambda}$ + M_U	3.1, 3.5, 2	2.6, 3.5, 2	2.6, 4.5, 3.25
$2M_\odot$ + NICER + $\tilde{\Lambda}_{\mathrm{BH}}$ + M_{gap}	4.9, 4.25, 2.75	4.8, 4.5, 3	4.5, 4.5, 3.25
$2M_\odot$ + NICER + $\tilde{\Lambda}_{\mathrm{BH}}$ + HESS	4.7, 4.25, 2.5	4.8, 4.75, 3	4.3, 5, 3.5

TABLE VI. Parameters of equations of state with the maximum posterior probability for different combinations of astrophysical measurements, using the DD2 hadronic EOS. Results for $m_\sigma = 600$ and $m_\sigma = 700$ MeV and for some combinations of astrophysical measurements were omitted due to the low statistics of stable and causal equations of state with these parameters.

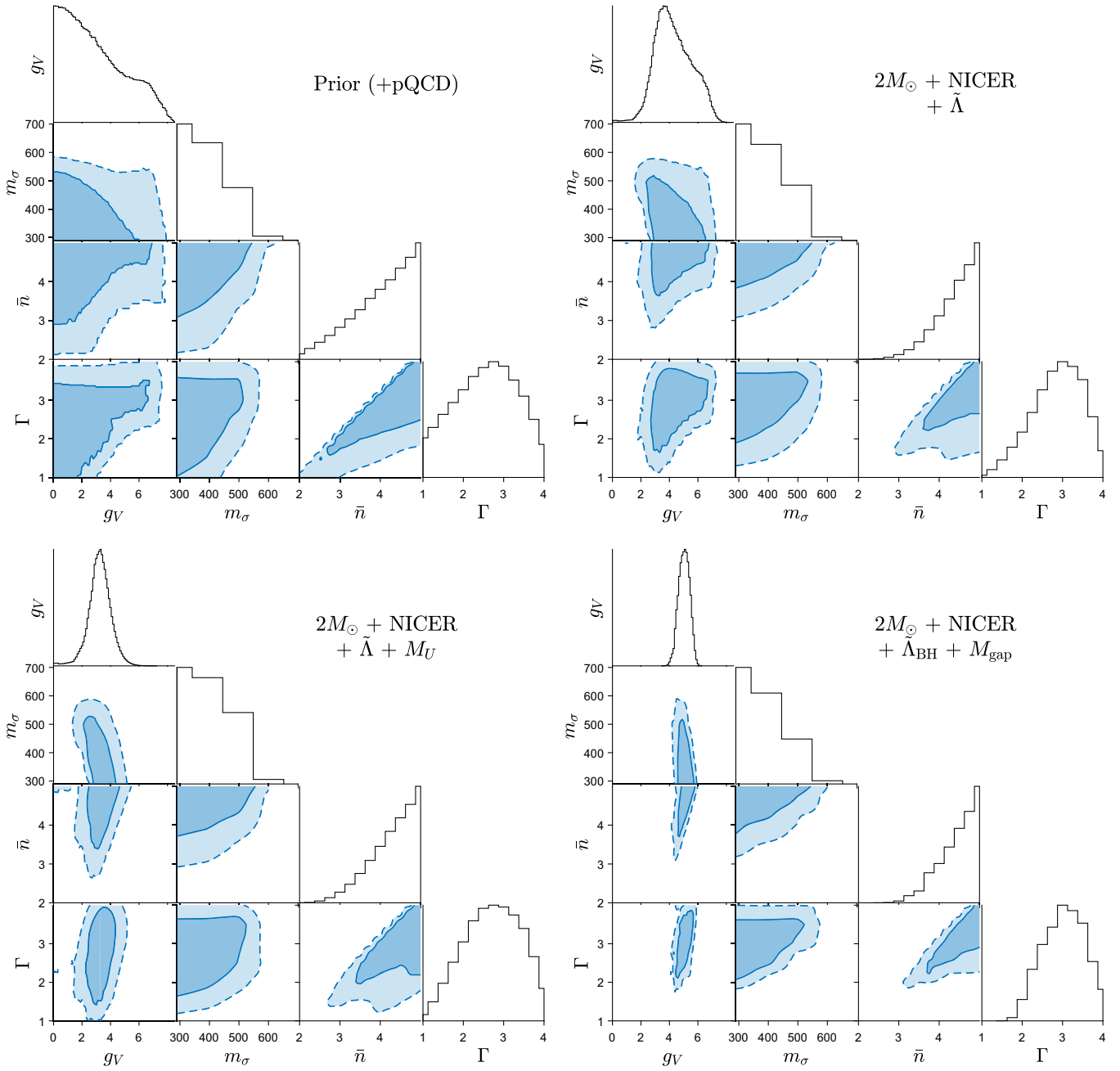| Measurement	$\vartheta_{\max}$: $(g_V, \bar{n}\ [n_0], \Gamma\ [n_0])$		
	$m_\sigma = 290$ MeV	$m_\sigma = 400$ MeV	$m_\sigma = 500$ MeV
$2M_\odot$ + NICER	6.7, 4.75, 2.75	6.1, 4.75, 2.75	5.5, 5, 3
$2M_\odot$ + NICER + $\tilde{\Lambda}$	4.4, 5, 3.75	4.1, 5, 3.75	5.5, 5, 3
$2M_\odot$ + NICER + $\tilde{\Lambda}$ + M_U	3.8, 5, 4	3.5, 5, 4	3.1, 5, 4

FIG. 13. Marginalized one- and two-dimensional priors and posteriors for selected combinations of astrophysical measurements. The PDFs were made using our complete EOS ensemble.

[1] J. Schaffner-Bielich, *Compact Star Physics* (Cambridge University Press, Cambridge, England, 2020), 10.1017/9781316848357.

[2] P. Demorest, T. Pennucci, S. Ransom, M. Roberts, and J. Hessels, Nature (London) **467,** 1081 (2010).

[3] J. Antoniadis *et al.*, Science **340,** 6131 (2013).

[4] Z. Arzoumanian *et al.* (NANOGrav Collaboration), Astrophys. J. Suppl. Ser. **235,** 37 (2018).

[5] H. T. Cromartie, S. M. R. E. Fonseca, and e. a. P. B. Demorest, Nat. Astron. **4,** 72 (2019).

[6] E. Fonseca *et al.*, Astrophys. J. Lett. **915,** L12 (2021).

[7] R. W. Romani, D. Kandel, A. V. Filippenko, T. G. Brink, and W. Zheng, Astrophys. J. Lett. **908,** L46 (2021).

[8] R. W. Romani, D. Kandel, A. V. Filippenko, T. G. Brink, and W. Zheng, Astrophys. J. Lett. **934,** L18 (2022).

[9] D. Kandel and R. W. Romani, Astrophys. J. **942,** 6 (2023).

[10] M. C. Miller, F. K. Lamb, A. J. Dittmann *et al.*, Astrophys. J. Lett. **887,** L24 (2019).

[11] T. E. Riley, A. L. Watts, S. Bogdanov *et al.*, Astrophys. J. Lett. **887,** L21 (2019).

[12] G. Raaijmakers, T. E. Riley, A. L. Watts *et al.*, Astrophys. J. Lett. **887,** L22 (2019).

[13] M. C. Miller *et al.*, Astrophys. J. Lett. **918,** L28 (2021).

[14] T. E. Riley *et al.*, Astrophys. J. Lett. **918,** L27 (2021).

[15] G. Raaijmakers, S. K. Greif, K. Hebeler, T. Hinderer, S. Nissanke, A. Schwenk, T. E. Riley, A. L. Watts, J. M. Lattimer, and W. C. G. Ho, Astrophys. J. Lett. **918,** L29 (2021).

[16] B. P. Abbott *et al.* (LIGO Scientific and Virgo Collaborations), Phys. Rev. Lett. **119,** 161101 (2017).

[17] B. P. Abbott *et al.* (LIGO Scientific and Virgo Collaborations), Phys. Rev. Lett. **121,** 161101 (2018).

[18] B. P. Abbott *et al.* (LIGO Scientific and Virgo Collaborations), Phys. Rev. X **9,** 011001 (2019).

[19] E. Annala, T. Gorda, A. Kurkela, and A. Vuorinen, Phys. Rev. Lett. **120,** 172703 (2018).

[20] E. R. Most, L. R. Weih, L. Rezzolla, and J. Schaffner-Bielich, Phys. Rev. Lett. **120,** 261103 (2018).

[21] S. De, D. Finstad, J. M. Lattimer, D. A. Brown, E. Berger, and C. M. Biwer, Phys. Rev. Lett. **121,** 091102 (2018); **121,** 259902(E) (2018).

[22] I. Tews, J. Margueron, and S. Reddy, Phys. Rev. C **98,** 045804 (2018).

[23] D. E. Alvarez-Castillo and D. B. Blaschke, Phys. Rev. C **96,** 045809 (2017).

[24] D. Blaschke, D. E. Alvarez-Castillo, A. Ayriyan, H. Grigorian, N. K. Largani, and F. Weber, Astrophysical aspects of general relativistic mass twin stars, arXiv:1906.02522.

[25] J.-E. Christian and J. Schaffner-Bielich, Astrophys. J. Lett. **894,** L8 (2020).

[26] J.-E. Christian and J. Schaffner-Bielich, Phys. Rev. D **103,** 063042 (2021).

[27] J.-E. Christian and J. Schaffner-Bielich, Astrophys. J. **935,** 122 (2022).

[28] T. Gorda, K. Hebeler, A. Kurkela, A. Schwenk, and A. Vuorinen, arXiv:2212.10576.

[29] E. Annala, T. Gorda, A. Kurkela, J. Nättilä, and A. Vuorinen, Nat. Phys. **16,** 907 (2020).

[30] M. Marczenko, L. McLerran, K. Redlich, and C. Sasaki, Phys. Rev. C **107,** 025802 (2023).

[31] C. Ecker and L. Rezzolla, Astrophys. J. Lett. **939,** L35 (2022).

[32] J.-L. Jiang, C. Ecker, and L. Rezzolla, Astrophys. J. **949,** 11 (2023).

[33] L. McLerran and S. Reddy, Phys. Rev. Lett. **122,** 122701 (2019).

[34] K. S. Jeong, L. McLerran, and S. Sen, Phys. Rev. C **101,** 035201 (2020).

[35] M. Leonhardt, M. Pospiech, B. Schallmo, J. Braun, C. Drischler, K. Hebeler, and A. Schwenk, Phys. Rev. Lett. **125,** 142502 (2020).

[36] J. Braun and B. Schallmo, Phys. Rev. D **105,** 036003 (2022).

[37] J. Braun, A. Geißel, and B. Schallmo, arXiv:2206.06328.

[38] J. N. Guenther, Eur. Phys. J. A **57,** 136 (2021).

[39] F. Attanasio, B. Jäger, and F. P. G. Ziegler, Eur. Phys. J. A **56,** 251 (2020).

[40] S. Borsányi, Z. Fodor, J. N. Guenther, R. Kara, S. D. Katz, P. Parotto, A. Pásztor, C. Ratti, and K. K. Szabó, Phys. Rev. Lett. **126,** 232001 (2021).

[41] A. Akmal, V. R. Pandharipande, and D. G. Ravenhall, Phys. Rev. C **58,** 1804 (1998).

[42] R. B. Wiringa, V. Fiks, and A. Fabrocini, Phys. Rev. C **38,** 1010 (1988).

[43] K. Hebeler, S. K. Bogner, R. J. Furnstahl, A. Nogga, and A. Schwenk, Phys. Rev. C **83,** 031301 (2011).

[44] S. Gandolfi, J. Carlson, S. Reddy, A. W. Steiner, and R. B. Wiringa, Eur. Phys. J. A **50,** 10 (2014).

[45] J. E. Lynn, I. Tews, J. Carlson, S. Gandolfi, A. Gezerlis, K. E. Schmidt, and A. Schwenk, Phys. Rev. Lett. **116,** 062501 (2016).

[46] I. Tews, J. Carlson, S. Gandolfi, and S. Reddy, Astrophys. J. **860,** 149 (2018).

[47] I. Tews, T. Krüger, K. Hebeler, and A. Schwenk, Phys. Rev. Lett. **110,** 032504 (2013).

[48] I. Tews, J. Margueron, and S. Reddy, Eur. Phys. J. A **55,** 97 (2019).

[49] P. Huovinen and P. Petreczky, Nucl. Phys. **A837,** 26 (2010).

[50] A. Bazavov *et al.* (HotQCD Collaboration), Phys. Rev. D **86,** 034509 (2012).

[51] A. W. Steiner, M. Hempel, and T. Fischer, Astrophys. J. **774,** 17 (2013).

[52] M. Hempel and J. Schaffner-Bielich, Nucl. Phys. **A837,** 210 (2010).

[53] S. Typel, G. Ropke, T. Klahn, D. Blaschke, and H. Wolter, Phys. Rev. C **81,** 015803 (2010).

[54] A. Kurkela, P. Romatschke, and A. Vuorinen, Phys. Rev. D **81,** 105021 (2010).

[55] S. Mogliacci, J. O. Andersen, M. Strickland, N. Su, and A. Vuorinen, J. High Energy Phys. 12 (2013) 055.

[56] T. Gorda, A. Kurkela, P. Romatschke, M. Säppi, and A. Vuorinen, Phys. Rev. Lett. **121,** 202701 (2018).

[57] M. Oertel, M. Hempel, T. Klähn, and S. Typel, Rev. Mod. Phys. **89,** 015007 (2017).

[58] Y. Nambu and G. Jona-Lasinio, Phys. Rev. **122,** 345 (1961).

[59] Y. Nambu and G. Jona-Lasinio, Phys. Rev. **124,** 246 (1961).

[60] T. Hatsuda and T. Kunihiro, Phys. Rep. **247,** 221 (1994).

[61] S. Gasiorowicz and D. A. Geffen, Rev. Mod. Phys. **41,** 531 (1969).

[62] P. Ko and S. Rudaz, Phys. Rev. D **50,** 6877 (1994).

[63] O. Ivanytskyi and D. B. Blaschke, Particles **5,** 514 (2022).

[64] O. Ivanytskyi and D. Blaschke, Phys. Rev. D **105,** 114042 (2022).

[65] D. Blaschke, U. Shukla, O. Ivanytskyi, and S. Liebing, Phys. Rev. D **107,** 063034 (2023).

[66] T. Hell, S. Rossner, M. Cristoforetti, and W. Weise, Phys. Rev. D **81,** 074034 (2010).

[67] K.-I. Kondo, Phys. Rev. D **82,** 065024 (2010).

[68] A. E. Radzhabov, D. Blaschke, M. Buballa, and M. K. Volkov, Phys. Rev. D **83,** 116004 (2011).

[69] M.-Z. Han, Y.-J. Huang, S.-P. Tang, and Y.-Z. Fan, Sci. Bull. **68,** 913 (2023).

[70] E. Annala, T. Gorda, J. Hirvonen, O. Komoltsev, A. Kurkela, J. Nättilä, and A. Vuorinen, arXiv:2303.11356.

[71] Z. Miao, A. Li, Z. Zhu, and S. Han, Astrophys. J. **904,** 103 (2020).

[72] W.-J. Xie and B.-A. Li, Phys. Rev. C **103,** 035802 (2021).

[73] D. Parganlija, P. Kovacs, G. Wolf, F. Giacosa, and D. H. Rischke, Phys. Rev. D **87,** 014011 (2013).

[74] P. Kovács, Z. Szép, and G. Wolf, Phys. Rev. D **93,** 114014 (2016).

[75] J. Takátsy, P. Kovács, Z. Szép, and G. Wolf, Universe **5,** 174 (2019).

[76] G. Kovács, P. Kovács, and Z. Szép, Phys. Rev. D **104,** 056013 (2021).

[77] A. Ayriyan, D. Alvarez-Castillo, D. Blaschke, and H. Grigorian, Universe **5,** 61 (2019).

[78] A. Ayriyan, D. Blaschke, A. G. Grunfeld, D. Alvarez-Castillo, H. Grigorian, and V. Abgaryan, Eur. Phys. J. A **57,** 318 (2021).

[79] A. Pfaff, H. Hansen, and F. Gulminelli, Phys. Rev. C **105,** 035802 (2022).

[80] G. A. Contrera, D. Blaschke, J. P. Carlomagno, A. G. Grunfeld, and S. Liebing, Phys. Rev. C **105,** 045808 (2022).

[81] S. Typel, M. Oertel, and T. Klähn, https://compose.obspm.fr.

[82] T. Krüger, I. Tews, K. Hebeler, and A. Schwenk, Phys. Rev. C **88,** 025802 (2013).

[83] G. Baym, C. Pethick, and P. Sutherland, Astrophys. J. **170,** 299 (1971).

[84] J. W. Negele and D. Vautherin, Nucl. Phys. **A207,** 298 (1973).

[85] M. Okamoto, T. Maruyama, K. Yabana, and T. Tatsumi, Phys. Lett. B **713,** 284 (2012).

[86] F. Douchin and P. Haensel, Astron. Astrophys. **380,** 151 (2001).

[87] P. Kovács, G. Kovács, and F. Giacosa, Phys. Rev. D **106,** 116016 (2022).

[88] P. Kovács, J. Takátsy, J. Schaffner-Bielich, and G. Wolf, Phys. Rev. D **105,** 103014 (2022).

[89] V. Abgaryan, D. Alvarez-Castillo, A. Ayriyan, D. Blaschke, and H. Grigorian, Universe **4,** 94 (2018).

[90] G. Baym, S. Furusawa, T. Hatsuda, T. Kojo, and H. Togashi, Astrophys. J. **885,** 42 (2019).

[91] K. Masuda, T. Hatsuda, and T. Takatsuka, Prog. Theor. Exp. Phys. **2013,** 073D01 (2013).

[92] D. Blaschke, E. O. Hanu, and S. Liebing, Phys. Rev. C **105,** 035804 (2022).

[93] R. C. Tolman, Phys. Rev. **55,** 364 (1939).

[94] J. Oppenheimer and G. Volkoff, Phys. Rev. **55,** 374 (1939).

[95] T. Hinderer, Astrophys. J. **677,** 1216 (2008).

[96] K. Yagi and N. Yunes, Phys. Rev. D **88,** 023009 (2013).

[97] T. Damour and A. Nagar, Phys. Rev. D **80,** 084035 (2009).

[98] S. Postnikov, M. Prakash, and J. M. Lattimer, Phys. Rev. D **82,** 024016 (2010).

[99] J. Takátsy and P. Kovács, Phys. Rev. D **102,** 028501 (2020).

[100] E. E. Flanagan and T. Hinderer, Phys. Rev. D **77,** 021502 (2008).

[101] P. Demorest, T. Pennucci, S. Ransom, M. Roberts, and J. Hessels, Nature (London) **467,** 1081 (2010).

[102] J. Antoniadis et al., Science **340,** 6131 (2013).

[103] H. T. Cromartie et al. (NANOGrav Collaboration), Nat. Astron. **4,** 72 (2019).

[104] E. Fonseca et al., Astrophys. J. Lett. **915,** L12 (2021).

[105] M. Linares, T. Shahbaz, and J. Casares, Astrophys. J. **859,** 54 (2018).

[106] M. C. Miller et al., Astrophys. J. Lett. **887,** L24 (2019).

[107] T. E. Riley et al., Astrophys. J. Lett. **887,** L21 (2019).

[108] M. C. Miller et al., Astrophys. J. Lett. **918,** L28 (2021).

[109] T. E. Riley et al., Astrophys. J. Lett. **918,** L27 (2021).

[110] E. Annala, T. Gorda, E. Katerini, A. Kurkela, J. Nättilä, V. Paschalidis, and A. Vuorinen, Phys. Rev. X **12,** 011058 (2022).

[111] W. Kastaun and F. Ohme, Phys. Rev. D **100,** 103023 (2019).

[112] P. Landry and R. Essick, Phys. Rev. D **99,** 084049 (2019).

[113] C. D. Capano, I. Tews, S. M. Brown, B. Margalit, S. De, S. Kumar, D. A. Brown, B. Krishnan, and S. Reddy, Nat. Astron. **4,** 625 (2020).

[114] T. Dietrich, M. W. Coughlin, P. T. H. Pang, M. Bulla, J. Heinzel, L. Issa, I. Tews, and S. Antier, Science **370,** 1450 (2020).

[115] A. Bauswein, O. Just, H.-T. Janka, and N. Stergioulas, Astrophys. J. Lett. **850,** L34 (2017).

[116] L. Rezzolla, E. R. Most, and L. R. Weih, Astrophys. J. Lett. **852,** L25 (2018).

[117] M. Shibata, S. Fujibayashi, K. Hotokezaka, K. Kiuchi, K. Kyutoku, Y. Sekiguchi, and M. Tanaka, Phys. Rev. D **96,** 123012 (2017).

[118] R. Abbott et al. (LIGO Scientific and Virgo Collaborations), Astrophys. J. Lett. **896,** L44 (2020).

[119] S. Huth et al., Nature (London) **606,** 276 (2022).

[120] S. Ghosh, D. Chatterjee, and J. Schaffner-Bielich, Eur. Phys. J. A **58,** 37 (2022).

[121] S. Ghosh, B. K. Pradhan, D. Chatterjee, and J. Schaffner-Bielich, Front. Astron. Space Sci. **9,** 864294 (2022).

[122] B. K. Pradhan, D. Chatterjee, R. Gandhi, and J. Schaffner-Bielich, Nucl. Phys. **A1030,** 122578 (2023).

[123] S. Shirke, S. Ghosh, and D. Chatterjee, Astrophys. J. **944,** 7 (2023).

[124] M. Omana Kuttan, J. Steinheimer, K. Zhou, and H. Stöcker, arXiv:2211.11670.

[125] S. Soma, L. Wang, S. Shi, H. Stöcker, and K. Zhou, J. Cosmol. Astropart. Phys. 08 (2022) 071.

[126] S. Soma, L. Wang, S. Shi, H. Stöcker, and K. Zhou, Phys. Rev. D **107,** 083028 (2023).

[127] D. Blaschke, A. Ayriyan, D. E. Alvarez-Castillo, and H. Grigorian, Universe **6,** 81 (2020).

[128] M. Agathos, J. Meidam, W. Del Pozzo, T. G. F. Li, M. Tompitak, J. Veitch, S. Vitale, and C. Van Den Broeck, Phys. Rev. D **92,** 023012 (2015).

[129] D. Wysocki, R. O'Shaughnessy, L. Wade, and J. Lange, arXiv:2001.01747.

[130] K. Chatziioannou, Gen. Relativ. Gravity. **52,** 109 (2020).

[131] M. C. Miller, C. Chirenti, and F. K. Lamb, Astrophys. J. **888,** 12 (2020).

[132] P. Landry, R. Essick, and K. Chatziioannou, Phys. Rev. D **101,** 123007 (2020).

[133] O. Komoltsev and A. Kurkela, Phys. Rev. Lett. **128,** 202701 (2022).

[134] T. Gorda, O. Komoltsev, and A. Kurkela, Astrophys. J. **950,** 107 (2023).

[135] T. Gorda, A. Kurkela, R. Paatelainen, S. Säppi, and A. Vuorinen, Phys. Rev. Lett. **127,** 162003 (2021).

[136] B. Margalit and B. D. Metzger, Astrophys. J. Lett. **850,** L19 (2017).

[137] A. Bauswein, T. W. Baumgarte, and H. T. Janka, Phys. Rev. Lett. **111,** 131101 (2013).

[138] S. Köppel, L. Bovard, and L. Rezzolla, Astrophys. J. Lett. **872,** L16 (2019).

[139] A. Bazavov *et al.* (HotQCD Collaboration), Phys. Rev. D **90,** 094503 (2014).

[140] V. Mykhaylova and C. Sasaki, Phys. Rev. D **103,** 014007 (2021).

[141] X.-Y. Wang, C. Dong, and Q. Wang, Phys. Rev. D **106,** 056027 (2022).

[142] P. Castorina, K. Redlich, and H. Satz, Eur. Phys. J. C **59,** 67 (2008).

[143] P. Braun-Munzinger, A. Kalweit, K. Redlich, and J. Stachel, Phys. Lett. B **747,** 292 (2015).

[144] D. E. Kharzeev, Phys. Rev. D **104,** 054015 (2021).

[145] X.-Y. Wang, F. Zeng, and Q. Wang, Phys. Rev. D **105,** 096033 (2022).

[146] E. Tiesinga, P. J. Mohr, D. B. Newell, and B. N. Taylor, Rev. Mod. Phys. **93,** 025010 (2021).

[147] P. J. Mohr, D. B. Newell, and B. N. Taylor, Rev. Mod. Phys. **88,** 035009 (2016).

[148] H. Gao and M. Vanderhaeghen, Rev. Mod. Phys. **94,** 015002 (2022).

[149] Y. Fujimoto, K. Fukushima, L. D. McLerran, and M. Praszalowicz, Phys. Rev. Lett. **129,** 252702 (2022).

[150] R. Negreiros, L. Tolos, M. Centelles, A. Ramos, and V. Dexheimer, Astrophys. J. **863,** 104 (2018).

[151] S. Weissenborn, I. Sagert, G. Pagliara, M. Hempel, and J. Schaffner-Bielich, Astrophys. J. Lett. **740,** L14 (2011).

[152] R. Nandi and P. Char, Astrophys. J. **857,** 12 (2018).

[153] R. Nandi and S. Pal, Eur. Phys. J. Spec. Top. **230,** 551 (2021).